Monthly Notices of the ROYAL ASTRONOMICAL SOCIETY

MNRAS **542,** 3354–3372 (2025) https://doi.org/10.1093/mnras/staf1433
Advance Access publication 2025 August 28

The ambiguous AT2022rze: changing-look AGN mimicking a supernova in a merging galaxy system

P. J. Pessi [1]★ R. Lunnan,[1] J. Sollerman [1] L. Yan,[2] A. Le Reste,[3] Y. Yao,[4,5] S. Nordblom,[6] Y. Sharma,[7] M. Gilfanov,[8,9] R. Sunyaev,[8,9] S. Schulze,[10] J. Johansson,[11] A. Gangopadhyay,[1] C. Fremling,[2,7] K. Tristram,[12] M. J. Hayes [1] C. Fransson,[1] Y. Hu [1] S. J. Brennan,[1] S. Rose,[13] K. De,[14] K-R. Hinds [15] C. Liu [10,16] A. A. Miller [10,16,17] Y-J. Qin [13] P. Charalampopoulos,[18] A. Gkini,[1] M. J. Graham [7] C. P. Gutiérrez [19,20] S. Mattila,[18,21] T. Nagao [18,22,23] I. Pérez-Fournon,[24,25] F. Poidevin,[24,25] J. S. Bloom,[5,26] J. Brugger,[2] T. X. Chen,[27] M. M. Kasliwal [7] F. J. Masci[27] and J. N. Purdum[2]

Affiliations are listed at the end of the paper

Accepted 2025 August 26. Received 2025 August 17; in original form 2025 May 29

ABSTRACT

AT2022rze is a luminous, ambiguous transient located south-east of the geometric centre of its host galaxy at redshift $z = 0.08$. The host appears to be formed by a merging galaxy system. The observed characteristics of AT2022rze are reminiscent of active galactic nuclei (AGNs), tidal disruption events, and superluminous supernovae. The transient reached a peak absolute magnitude of -20.2 ± 0.2 mag, showing a sharp rise ($t_{\rm rise,1/e} = 27.5 \pm 0.6$ d) followed by a slow decline ($t_{\rm dec,1/e} = 382.9 \pm 0.6$). Its bumpy light curve and narrow Balmer lines indicate the presence of gas (and dust). Its light curve shows rather red colours, indicating that the transient could be affected by significant host extinction. The spectra reveal coronal lines, indicative of high-energy (X-ray/UV) emission. Archival data reveal no prior activity at this location, disfavouring a steady-state AGN, although an optical spectrum obtained prior to the transient is consistent with an AGN classification of the host. Based on this, we conclude that the transient most likely represents a changing-look AGN at the centre of the smallest component of the merging system.

Key words: galaxies: active – galaxies: interactions – transients: supernovae – transients: tidal disruption events.

1 INTRODUCTION

Transient astronomical events provide critical insights into the dynamic processes of the universe. Modern high-cadence, all-sky surveys have dramatically enhanced our ability to detect and study a broad range of transient phenomena, many of which display complex and often puzzling observational characteristics. Among these, transients displaying extreme luminosity variations are particularly challenging to interpret, as the energy required to power them often pushes the boundaries of standard theoretical models. Three prominent classes of such energetic transients are superluminous supernovae (SLSNe), tidal disruption events (TDEs), and changing-look active galactic nuclei (CLAGNs).

Core collapse supernovae (CCSNe) mark the explosive deaths of massive stars ($> 8M_{\odot}$). CCSNe can be classified by spectroscopic and/or photometric features (e.g. Gal-Yam 2017). In particular, events that display exceptionally high peak luminosities, typically brighter than ~ -20 mag in optical bands, are classified as SLSNe (e.g. Gal-Yam 2019). When hydrogen (H) lines are visible in the spectra of these events, they are classified as Type II SLSNe or Type IIn SLSNe if the hydrogen features are narrow, which indicates interaction between the supernova (SN) ejecta and a dense circumstellar material (CSM, e.g. Smith 2017). TDEs occur when a star intersects the tidal radius of a black hole (BH) and is torn apart by tidal forces, producing a luminous flare powered by the fallback and accretion of stellar debris (e.g. Gezari 2021). Active galactic nuclei (AGNs) are sustained by accretion of gas on to supermassive BHs (SMBHs) at galactic centres, producing intense, persistent emission across the electromagnetic spectrum (e.g. Padovani et al. 2017). A subclass of AGNs have been discovered to change their aspect and/or ignite when their host galaxies transition from quiescence to active accretion into the central BH, displaying luminous, energetic light curves. These have been labelled changing-look AGN (CLAGN; e.g. Ricci & Trakhtenbrot 2023).

In most cases, distinguishing SLSNe, TDEs, and AGNs is relatively straightforward by spectral matching or light curve analysis (a large variety of classification tools exits, here we only list a small fraction as example: Howell et al. 2005; Blondin & Tonry 2007; Narayan et al. 2018; Muthukrishna, Parkinson & Tucker 2019; Förster et al. 2021; Fraga et al. 2024). For instance, AGN variability is generally stochastic and persistent, unlike the more defined temporal structure of SLSNe and TDEs. TDEs typically appear blue and exhibit little colour evolution, whereas SLSNe begin with high temperatures and gradually redden as they cool. On the contrary, CLAGNs are very diverse, and their characteristics can resemble those of SLSNe IIn and TDEs (e.g. Komossa & Grupe 2024).

★ E-mail: priscila.pessi@astro.su.se

Recent studies have started to incorporate host galaxy properties alongside photometric behaviour to aid in classification (e.g: Gomez et al. 2020; Gagliano et al. 2023). However, overlap in host galaxy location, particularly for events located in nuclear or circumnuclear regions, makes classification even more ambiguous (e.g. French et al. 2020; Grishin et al. 2021; Ward et al. 2021; Li et al. 2023). Additionally, dust and gas surrounding the transient may produce prolonged, bumpy, and luminous light curves, further obscuring classification. As a result SLSNe, TDEs, and (CL)AGNs can become contaminants in corresponding sample studies (see e.g. the contaminants in the SLSN II sample presented by Pessi et al. 2025).

There is an increasing number of energetic transients with ambiguous characteristics being discovered (e.g. Kankare et al. 2017). A large fraction of these events is found at the nuclei of their host galaxies and have been dub these events ambiguous nuclear transients (ANTs; Wiseman et al. 2025). ANTs exhibit heterogeneous spectral and photometric properties that do not really fit those of SLSNe, TDEs, or AGNs. Mid-infrared (MIR) observations suggest that dust and molecular gas may shape the optical properties of ANTs, highlighting the need for multiwavelength observations to understand their nature. AT2022rze exemplifies this ambiguity. It appears centrally located in a compact structure, possibly a small galaxy merging with a larger host, but exhibits properties that defy a straightforward classification.

Understanding enigmatic events is critical, not only for improving the classification framework of transient populations but also for understanding the physical mechanisms powering these phenomena. This study focuses on the analysis of AT2022rze, a puzzling event originally classified as an SN, but exhibiting characteristics similar to CLAGNs and TDEs. The observations of AT2022rze are presented in Section 2. These are analysed in Section 3, and the results of the analysis are discussed in Section 4. We conclude in Section 5.

2 OBSERVATIONS

The discovery of AT2022rze (also known as Gaia22dmp, ZTF22abnfjsm, and ATLAS22bmgb) was reported on 2022 August 21 by Hodgkin et al. (2022). Its location at RA $= 12^{h}22^{m}52\overset{s}{.}16$, Dec. $= +76°02'47\overset{''}{.}26$, (J2000.0) allows the identification of the galaxy WISEAJ122252.07+760253.9 as the host. AT2022rze is located at the centre of a small luminous 'blob' (galaxy B, see Section 3.3) located south-east from the geometrical centre of the host (see Fig. 1, see Section 3.3 for further discussion of the host). AT2022rze was classified as a SN IIn almost 4 months after its discovery, on December 1 2022, by Hinds et al. (2022). Two years later, on December 16 2024, it was re-classified as an AGN by (Gagliano 2024). Both classifications are based on spectroscopic features, raising questions about the true nature of this event.

From the position of the hydrogen emission lines, we derive a redshift of $z = 0.082$, consistent with the reported photometric redshift of the host (Bilicki et al. 2014). We employ the `astropy.cosmology` software adopting $H_0 = 73$ km s^{-1} Mpc^{-1}, $\Omega_{\rm Matter} = 0.27$, $\Omega_{\rm Lambda} = 0.73$ as cosmological parameters. With these, we obtain a distance modulus of $\mu = 37.76$ mag. We do not consider uncertainties related to host galaxy peculiar velocities as it is in the *Hubble* flow ($z > 0.02$) and corrections would be small. From the NASA/IPAC Extragalactic Database's (NED[1]), we obtain a Milky Way (MW) extinction of $A_V = 0.123$ mag. We use NED's Galactic Extinction Calculator,[2] accessed through the `ned_extinction_calc` script[3] to obtain the MW extinction in different photometric bands. The effective wavelength corresponding to each filter was obtained from the Spanish Virtual Observatory (SVO) filter information service (Rodrigo, Solano & Bayo 2012; Rodrigo & Solano 2020). We do not consider host extinction, although see Section 3.3. The available photometric and spectroscopic data are presented below.

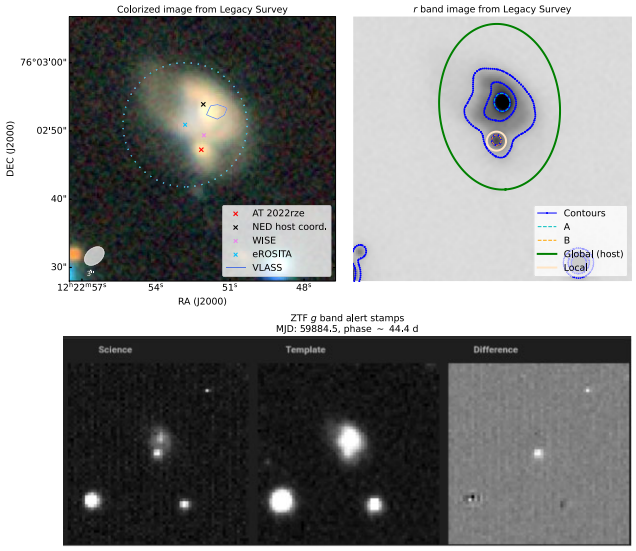

Figure 1. Host images. Top left panel: colourized Legacy Survey (Dey et al. 2019) cut-out centred on AT2022rze. The position of the transient is marked with a red cross. The coordinates of the host as obtained from NED are shown with a black cross. A purple cross shows the coordinates of the AllWISE observations. A light blue cross shows the coordinates of the eROSITA observations, a dotted circle of the same colour with a 9.1 arcsec radius shows the 98 per cent error radius for these observations. Tentative VLASS radio continuum emission is shown as a blue contour. The grey ellipse marks the size of the VLASS beam. Top right panel: r-band Legacy Survey cutout centred on AT2022rze. A green and salmon circle denote the respective global and local regions considered for host characterization. Blue markers show constant value pixel contours. Cyan and orange dashed ellipses mark the respective fits to the smallest regions confined by the contours. For details, see Section 3.3. Bottom panel: Stamps associated with a ZTF g-band detection alert. Science, Template, and Difference of those, respectively. These were obtained from the Alerce broker (https://alerce.online/, Förster et al. 2021).

2.1 Photometry

AT2022rze was detected by the public surveys carried out with the *Gaia* satellite (Gaia Collaboration 2016), the Asteroid Terrestrial-impact Last Alert System (ATLAS; Tonry et al. 2018; Smith et al. 2020), and the Zwicky Transient Facility (ZTF; Bellm et al. 2019a; Graham et al. 2019; Masci et al. 2019; Dekany et al. 2020). Thus, it has extensive optical photometric follow-up. Additional photometric follow-up was obtained as part of the ZTF collaboration with the

[1]The NED is funded by the NASA and operated by the California Institute of Technology.

[2]NED's Extinction Calculator considers the recalibration presented by Schlafly & Finkbeiner (2011) to the extinction map presented by Schlegel, Finkbeiner & Davis (1998), assuming a Fitzpatrick (1999) reddening law with $R_{\rm v} = 3.1$.

[3]https://github.com/mmechtley/ned_extinction_calc

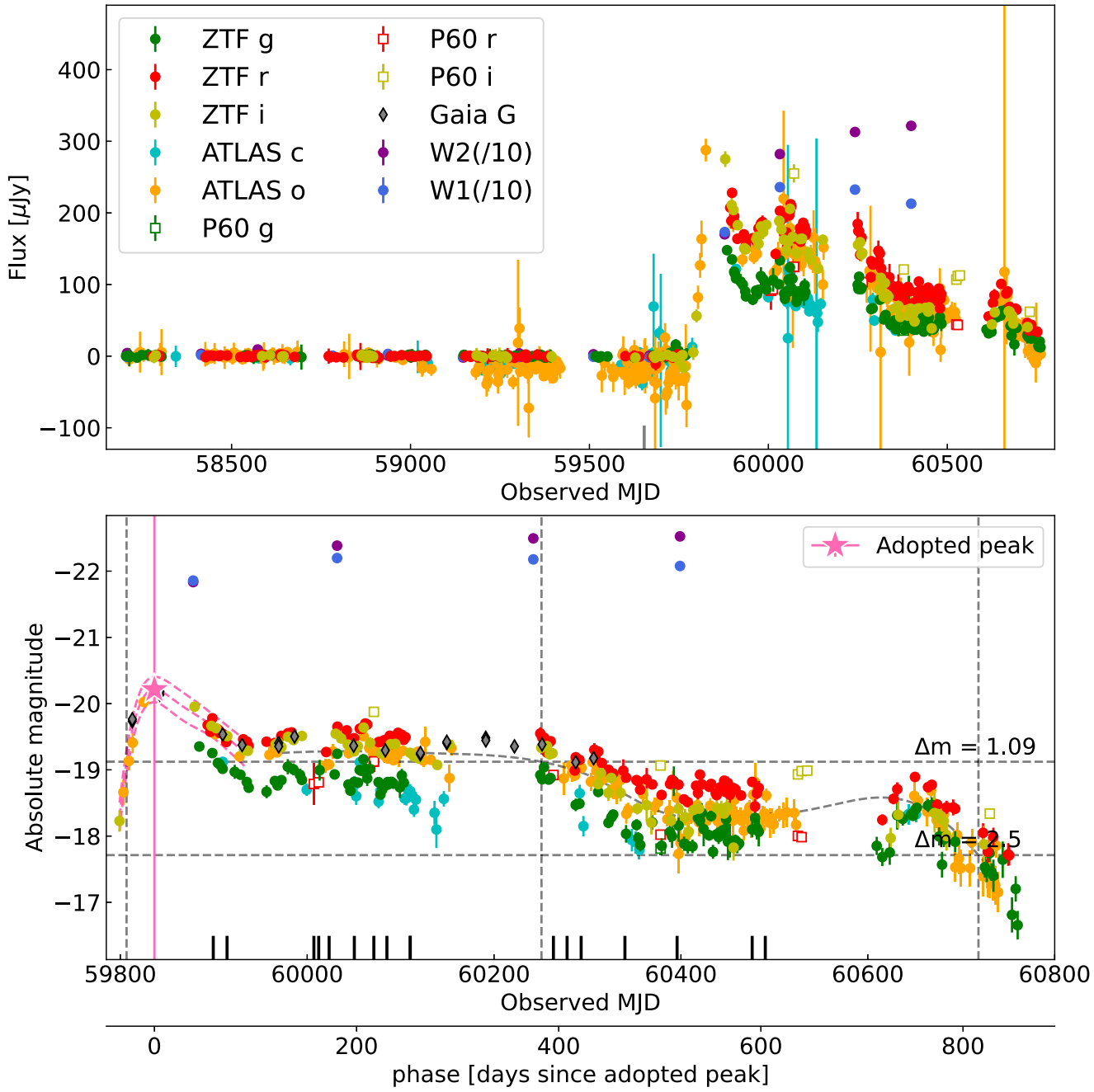

Figure 2. Top panel: Observed flux. *WISE* flux (but not absolute magnitude) is scaled by a factor 10 for better visibility. Bottom panel: Absolute magnitudes. Green, red, and yellow circles represent the ZTF *gri* bands, respectively. Cyan and orange circles represent the ATLAS *co* bands, respectively. P60 SEDM *gri* observations in the SDSS system are represented as green, red and yellow empty squares, respectively. Black rhomboids represent the *Gaia G* band. Dark magenta and dark blue circles show the *WISE W*2 and *W*1 bands, respectively. The central dashed pink line in the bottom panel indicate the Gaussian Process interpolation to the earlier portion of the light curve used to estimate the peak epoch, shown as a pink star, the top and bottom dashed pink lines indicate the associated interpolation confidence interval (see Section 3.1.1). The central dashed grey line shows the ALR interpolation after peak. Vertical and horizontal grey dashed lines indicate the rise and decline times. Short vertical lines on the *x*-axis indicate epochs of spectroscopic observations.

Spectral Energy Distribution Machine (SEDM; Blagorodnova et al. 2018) on the 60-inch telescope (P60) at Palomar Observatory. Moreover, MIR observations were obtained by the *Wide-field Infrared Survey Explorer* (*WISE*) instrument.

The observed photometry is listed in Tables A1–A3. The corresponding light curves are shown in Fig. 2. Absolute magnitudes are obtained as $M_\lambda = m_\lambda - \mu - A_\lambda - K\_corr$, where m_λ is apparent magnitude in the AB system, $\mu = 37.76$ mag is the distance modulus (see Section 1), A_λ is the MW extinction in the considered band, and K_corr is the cosmological term for the K-correction (Hogg et al. 2002) obtained as $-2.5 \times \log(1+z)$ (as presented in Chen et al. 2023 and Pessi et al. 2025).

2.1.1 *Gaia*

The Gaia Science Alerts project (Hodgkin et al. 2021) is dedicated to search for transient events within Gaia data. Alerts for discovered transients are made public through *Gaia* alerts that provide information about the transient, including the average magnitude of the source across all CCD strips at each considered timestamp. We obtained the public light curve from the dedicated repository.[4] The estimated absolute magnitudes are presented as black rhomboids in the bottom panel of Fig. 2. Since the public light curves do not include associated error bars, we do not include error bars here.

2.1.2 *ATLAS*

The ATLAS survey scans the sky in two wide filters: c (or 'cyan' band, in the wavelength range 4200–6500 Å, roughly corresponding to the typical $g + r$ range), and o (or 'orange' band, in the wavelength range of 5600–8200 Å, roughly corresponding to the typical $r + i$ range); with a cadence of around 2 d (Smith et al. 2020; Shingles et al. 2021). We retrieved the ATLAS forced-photometry from the dedicated repository.[5], and processed it utilizing the suggested pipeline developed by Young (2020), with the intra-night stacking option. The c and o light curves are presented in flux and absolute magnitude in the top and bottom panels of Fig. 2, respectively.

2.1.3 *ZTF*

ZTF is a wide-field (47-square-degree field of view), high-cadence survey (minutes to days, with a 3 d average for the public survey; Bellm et al. 2019b), which covers the whole northern sky. ZTF forced point-spread function (PSF) photometry is processed and distributed by the Science Data System at IPAC[6] (Masci et al. 2019). We requested the available forced photometry following the steps outlined in the ZTF forced photometry guideline.[7] We process the retrieved light curves in the same way as outlined by Pessi et al. (2025), removing points with bad quality flags and finding the zero flux baseline corresponding to each filter. The gri light curves are presented in flux and absolute magnitude in the top and bottom panels of Fig. 2, respectively.

We obtained further P60 photometry through the ZTF collaboration. Photometry is obtained through PSF fitting, calibrated with standard stars from the Sloan Digital Sky Survey (SDSS, Gunn 1995). All the photometry is processed using the FPIPE software (Fremling et al. 2016) using SDSS reference images. The P60 photometry is neither colour-corrected nor adjusted for differences in filter response. Although we do not use these measurements in our analysis, we include them here for completeness.

2.1.4 *WISE*

The field of AT2022rze was observed with *WISE* in the $W1$ and $W2$ bands (with central wavelengths of 3.4 and 4.6 μm, respectively) during the NEOWISE-reactivation mission (NEOWISE-R; Mainzer et al. 2014). Single exposures in the $W1$ and $W2$ bands were collected from the NASA/IPAC Infrared Science Archive (IRSA) and coadded using the ICORE service (Masci 2013). Reference images were created by coadding data from 2015, which were subtracted from the subsequent images. We perform aperture photometry on the subtracted images using a standard 8.25 arcsec radius aperture (and corresponding aperture corrections), and zero magnitude fluxes for the *WISE* $W1$ and $W2$ bands of $F_{\nu,0}^{W1} = 306.7$ Jy and $F_{\nu,0}^{W2} = 170.7$ Jy (Wright et al. 2010a).

Table 1. MIR observations obtained from the AllWISE Source Catalog. The magnitudes are presented in the Vega system. Error bars associated with each filter are presented in anal

	$W1$ (mag)	$W2$ (mag)	$W3$ (mag)	$W4$ (mag)
Host	13.614 (0.039)	13.382 (0.044)	9.433 (0.045)	7.542 (0.197)
Other	13.878 (0.048)	13.563 (0.050)	9.895 (0.064)	7.820 (0.251)

2.1.5 *Host*

The host galaxy has been observed by the *WISE* mission (Wright et al. 2010b), the Very Large Array Sky Survey (VLASS; Lacy et al. 2020; Gordon et al. 2021), and eROSITA (Predehl et al. 2021). We note that the host is formed by two galaxies undergoing a merging event, namely galaxy A and galaxy B (see Fig. 1 and Section 3.3 for a detailed description). Throughout this work, we refer to the entire system as the host, specifying galaxy A or B when relevant.

MIR observations of the host are available in the AllWISE Source Catalog.[8] AllWISE combines both the WISE cryogenic and NEOWISE (Mainzer et al. 2011) post-cryogenic survey phases, providing observations at 3.4, 4.6, 12, and 22 μm, corresponding to the so-called $W1$, $W2$, $W3$, and $W4$ filters, respectively. A coordinate search considering a 10 arcsec cone radius retrieves two sources, one consistent with the NED coordinates of the host, and the other offset 0.4 arcsec W, 4.5 arcsec S from that position (see Fig. 1, see Section 3.3 for further discussion). The magnitudes in each of the *WISE* filters are listed in Table 1.

Radio observations of the host are available in the VLASS archive.[9] We retrieve quick look single epoch radio continuum images from the VLASS, centred on the position of AT2022rze. These images sample the radio continuum between 2 and 4 GHz, and were taken on 2017 September 15, 2020 September 3, and 2023 March 5. We tentatively detect radio continuum emission (2.5σ) close to the NED coordinates of the host in the epoch 1 and 3 images, but do not find emission at the position of AT2022rze. In order to increase the signal-to-noise ratio of the images, we stack the three epochs together, coadding the images weighted by their rms (0.12, 0.15, and 0.11 mJy beam^{-1}, respectively). In the stacked image, we detect the 3 GHz radio continuum emission from the host with flux density 0.653 ± 0.2 mJy. We do not detect radio emission from AT2022rze, but derive a 3σ upper limit $S_{3GHz} < 0.2$ mJy within the beam (∼3 arcmin), assuming radio continuum emission from the source is unresolved.

Observations by eROSITA performed between 2020 and 2021 (before the transient went off), detected the faint X-ray source SRGe J122252.8+760251, located at RA = 185.72006°, Dec. = 76.047474°. The radius of the localization region (at the 98 per cent confidence level) is 9.1 arcsec (see Fig. 1).

[4] https://gsaweb.ast.cam.ac.uk/alerts/
[5] https://fallingstar-data.com/forcedphot/
[6] Formerly referred to as the Infrared Processing & Analysis Center (https://www.ipac.caltech.edu).
[7] http://web.ipac.caltech.edu/staff/fmasci/ztf/forcedphot.pdf
[8] https://wise2.ipac.caltech.edu/docs/release/allwise/
[9] http://cutouts.cirada.ca/

2.2 Spectroscopy

In addition to the photometric follow up, we obtained several epochs of spectroscopic observations using the SEDM spectrograph, the Spectrograph for the Rapid Acquisition of Transients (SPRAT, Piascik et al. 2014) at the 2-m Liverpool Telescope, the Low-Resolution Imaging Spectrograph (LRIS, Oke et al. 1995) at the 10-m Keck I telescope, the Alhambra Faint Object Spectrograph and Camera (ALFOSC) at the Nordic Optical Telescope, and the Double Spectrograph (DBSP, Oke & Gunn 1982) at the Palomar 200-inch telescope. The SEDM spectra were reduced using the `pysedm` fully automated integral field spectrograph pipeline (Rigault et al. 2019; Kim et al. 2022). SPRAT spectra were reduced using an adaptation of the `FRODOspec` pipeline (Barnsley, Smith & Steele 2012). LRIS spectra were reduced using the `LPipe` automated reduction pipeline (Perley 2019). ALFOSC spectra were reduced using the `PypeIt` python spectroscopic data reduction pipeline (Prochaska et al. 2020a; Prochaska et al. 2020b). DBSP spectra were reduced using the `DBSP_DRP` automated spectroscopic data reduction pipeline (Mandigo-Stoba, Fremling & Kasliwal 2022). Follow-up observations were coordinated using the Fritz instance of SkyPortal (van der Walt, Crellin-Quick & Bloom 2019; Coughlin et al. 2023). The log of spectroscopic observations can be found in Table B1. The obtained spectral evolution is shown in Fig. 3.

Most of the spectra were obtained with the slit aligned along the parallactic angle to minimize atmospheric dispersion effects. The ALFOSC spectra obtained at 422.2 and 465.5 d were observed with a slit rotation that allowed to include both the transient (located at the centre of galaxy B) and galaxy A (see Section 3.3) and thus, obtain two spectral epochs of the latter. These are shown in Fig. 7.

The position of the transient (i.e. galaxy B) was also observed by the Dark Energy Spectroscopic Instrument (DESI, DESI Collaboration 2016a, b) on 2022 March 15, ∼5 months before the transient was discovered. The spectrum is included in their recent data release (DESI Collaboration 2025) and we include it in Fig. 7.

3 ANALYSIS

AT2022rze was originally classified as a SN IIn. Because of its peak absolute magnitude, it is included in the SLSN II sample presented by Pessi et al. (2025). AT2022rze does not stand out from the rest of the SLSN II sample. However, Pessi et al. (2025) only include observations up to December 12th 2022, an arbitrary date that could result in missed light curve characteristics. This event was re-classified as an AGN in December 16th 2024. Thus, we go back to AT2022rze and find that its light curve continues to show activity for over 700 d after peak. Yet, there is an apparent lack of evolution of the spectral lines that resulted in the original SN classification, suggesting that such classification could still be valid. In the following, we analyse the available observations in order to decipher the true nature of this transient.

3.1 Light curve

Although the reported discovery date of AT2022rze is August 21st 2022 (MJD = 59812.8), we can see in the bottom panel of Fig. 2 that the transient was first detected on August 8th 2022 (MJD = 59799.18) in the ZTF i band at -18.2 ± 0.2 mag. The top panel of Fig. 2 shows the measured historical flux at the position of the target since March 28th 2018 (MJD = 58205.3). We can see that the historical optical and NIR light curves show no flux variations until the first ZTF i band detection, meaning that there was no transient event at the time, or at least, no optical activity brighter than the surveys limiting magnitude.

3.1.1 *Light curve peak and time-scales*

The gaps in observations around the first peak prevent an accurate estimate of the peak epoch in any given filter. Given the overlap between the rio and G filters, we consider no colour evolution around the time of peak, and include the observations in all these bands to estimate an overall approximate peak epoch. To do this, we use Gaussian Process (GP, e.g: Rasmussen & Williams 2006) to interpolate the observations that cover the main (more luminous) light curve peak in the mentioned filters. GP is implemented utilizing the `GPY` python package.[10] We consider the epoch and absolute magnitude of the peak of the GP median to be the peak epoch and peak absolute magnitude of AT2022rze. Error bars represent the standard deviation of the estimated peak of the median of 1000 posterior samples. The interpolation together with the confidence region is shown as dashed pink lines in the bottom panel of Fig. 2. The adopted peak epoch is MJD = 59836.5 ± 2.4, and the adopted peak absolute magnitude is -20.2 ± 0.2 mag, shown as a pink star in the bottom panel of Fig. 2. Since the interpolation considers rio and G, this peak epoch does not correspond to a single band, but we would associate the peak with the o band, as this is the filter with the wider passband and the most observations in the considered region. All the phases in this work are presented as rest frame days with respect to the adopted peak, unless stated otherwise.

Pessi et al. (2025) follows the work of Chen et al. (2023) and define rise and decline time-scales as flux fractions with respect to peak. The considered fractions are 10 per cent and 1/e, which correspond to Δmag = 2.5 and Δmag = 1.09, respectively. Dashed grey horizontal lines in Fig. 2 indicate the considered Δmag's. Using the GP interpolation described above, we can estimate a 1/e rise time $t_{\rm rise,1/e} = 27.5 \pm 0.6$ d. $t_{\rm rise,10\ per\ cent}$ cannot be determined due to the lack of early observations. We can see that the light curve shows many wiggles and bumps after peak, it also has several gaps in the observations. Thus, GP interpolation is not ideal to interpolate the whole light curve. Instead, we interpolate the post-peak o band light curve using the Automated Loess Regression (`ALR`) pipeline presented by Rodríguez et al. (2019). The resulting interpolation is presented as a grey-dashed line in Fig. 2. We use this `ALR` interpolation to determine the decline time-scales $t_{\rm dec,1/e}$ and $t_{\rm dec,10\ per\ cent}$, which are 382.9 ± 0.6 and 815.2 ± 0.6 d, respectively.

These rise times of AT2022rze are comparable to the rise times presented for SLSNe II by Pessi et al. (2025). They report a median $t_{\rm rise,1/e}$ of 33.8, 37.0, and 46.9 d in the gri bands, respectively. On the contrary, the decline times of AT2022rze are much longer than those presented for SLSNe II. The median $t_{\rm dec,1/e}$ of SLSNe II being 75.0, 89.3 and 98.3 d in the gri bands, respectively; and the median $t_{\rm dec,10\ per\ cent}$ being 235.8, 248.1, and 246.8 d in the gri bands, respectively. However, Pessi et al. (2025) find that a fraction of slow declining SLSNe II exist (∼ 5 per cent of their sample), that take over a year to fade.

3.1.2 *Colour evolution*

The full ZTF gr band light curves of AT2022rze were interpolated with `ALR`. These interpolations were used to construct the $g-r$ colour curve presented in Fig. 4. We compare the observed colour of

[10] https://gpy.readthedocs.io/en/deploy/.

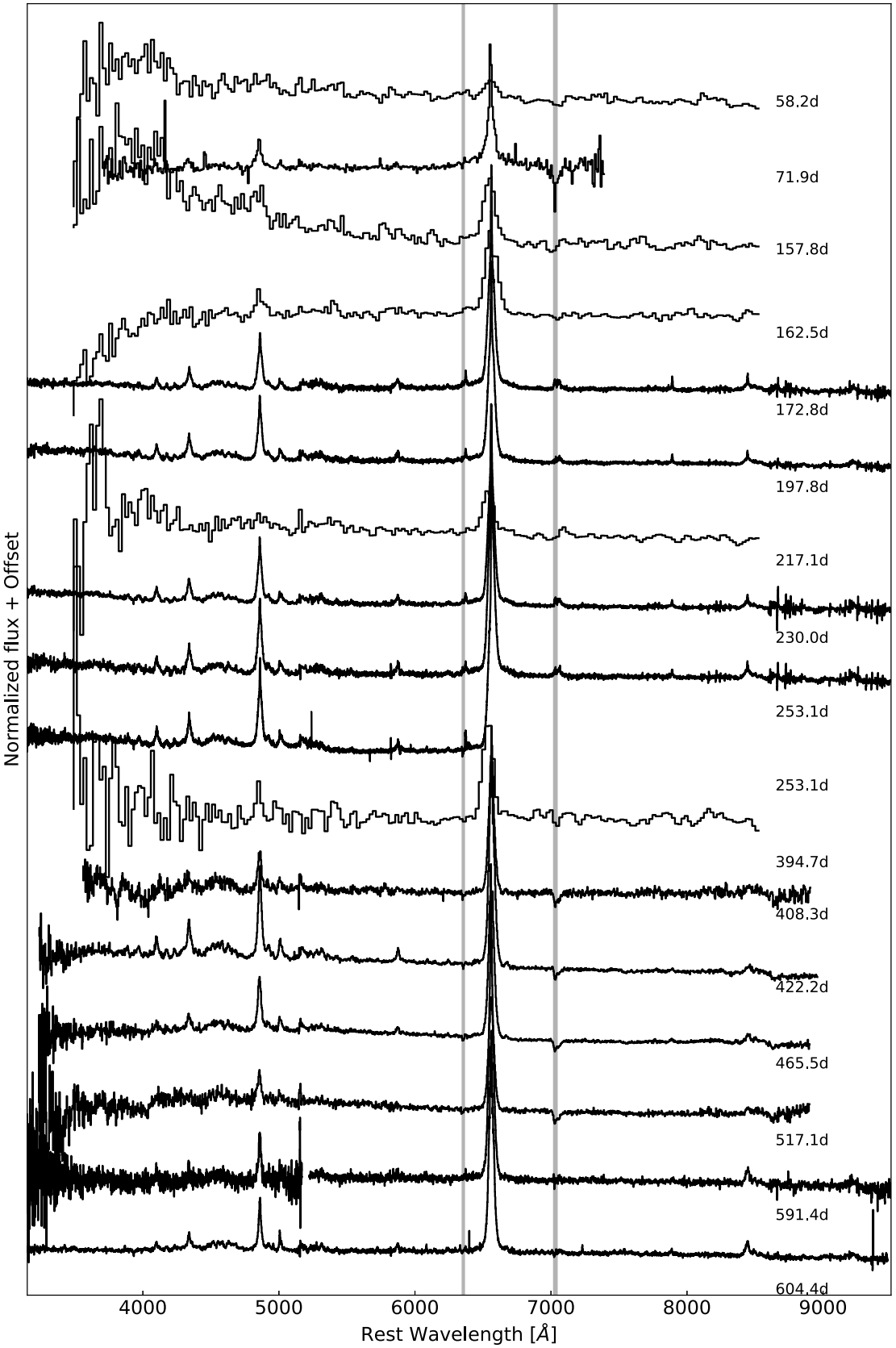

Figure 3. Spectral evolution of AT2022rze. The vertical grey stripes mark the telluric affected regions. Specific spectral lines are identified in Fig. 6. To the right of each spectrum we annotate the spectral rest frame phase with respect to light curve peak (see Section 3.1.1).

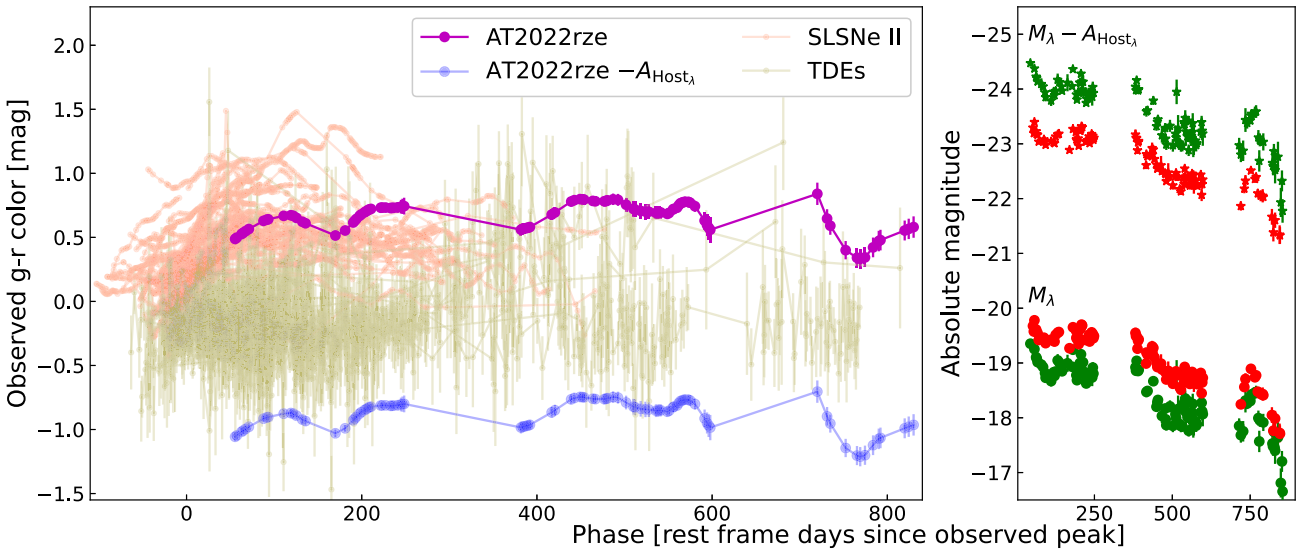

Figure 4. Left panel: $g - r$ colour evolution of AT2022rze (magenta) compared to the same colours of the SLSN II sample (salmon) presented by Pessi et al. (2025) and the sample of TDEs presented by Yao et al. (2023). In blue, we show the respective colour of AT2022rze when considering host extinction (see Section 3.3). Right panel: ZTF g and r band absolute magnitude light curves in green and red, respectively. Round markers show the absolute magnitude light curves obtained as described in Section 2.1. Star markers show the absolute magnitude light curves obtained considering substantial host extinction (see Section 3.3).

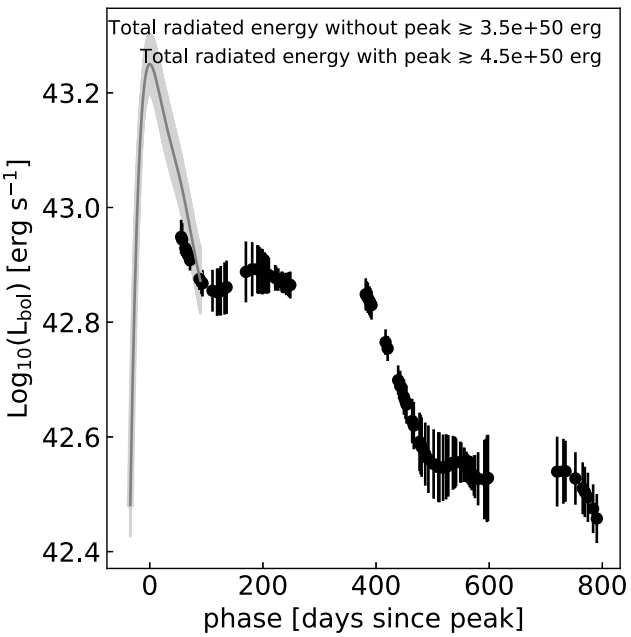

Figure 5. AT2022rze pseudo-bolometric light curve. Black markers show the light curve estimated using only *gri* bands. The solid grey curve shows the peak estimated using BC_o on the early time GP interpolation.

AT2022rze to those of the SLSN II sample presented by Pessi et al. (2025) and to those of TDEs presented by Yao et al. (2023). We find better agreement with SLSNe II (although see Section 3.3). We note that we do not have colour information before or around peak, but the evolution at the earliest observed phases seem to follow the trend of the SLSN II sample.

3.1.3 Pseudo-bolometric light curve

To constrain the total radiated energy we construct the pseudo-bolometric light curve of AT2022rze. We only consider ZTF *gri* observations. To have a consistent estimate of the spectral energy distribution (SED) during the evolution of the event, we only consider epochs in which all three bands were observed. The SED is estimated by interpolating the *gri* bands with respect to the adopted peak epoch using `ALR`, and integrating over the resulting interpolated curve. The obtained light curve is presented in Fig. 5. This approach only provides a lower limit for the bolometric luminosity as it completely ignores UV and IR contributions to the SED, as well as the effect of host galaxy extinction. Still, it allow us to place a lower limit on the total radiated energy, which we estimate to be $E_{\mathrm{rad}} \gtrsim 3.5 \times 10^{50}$ erg.

Although the peak of the light curve was missed in the *gri* bands, it was observed in the *o* band. We note that there is some overlap between the first *gri* observations and the earlier *o*-band photometry. We decided to consider this overlapping region to estimate a bolometric correction as

$$\mathrm{BC}_o = -2.5 \times \log(L_{\mathrm{bol}}/L_o), \quad (1)$$

where BC_o is the bolometric correction in the *o* band, L_{bol} is the estimated pseudo-bolometric luminosity and L_o is the luminosity in the *o* band. Once we obtained BC_o, we consider the GP interpolation described in Section 3.1.1 to represent the *o* band at earlier times, and convert it to pseudo-bolometric luminosity through the estimated BC_o. The solid grey curve in Fig. 5 shows the additional peak. The total radiated energy when considering this light curve is $E_{\mathrm{rad}} \gtrsim 4.5 \times 10^{50}$ erg. The complete pseudo-bolometric light curve is presented in Table A4.

3.2 Spectra

The spectral evolution of AT2022rze is presented in Fig. 3. The first available spectrum has low resolution and was observed ∼

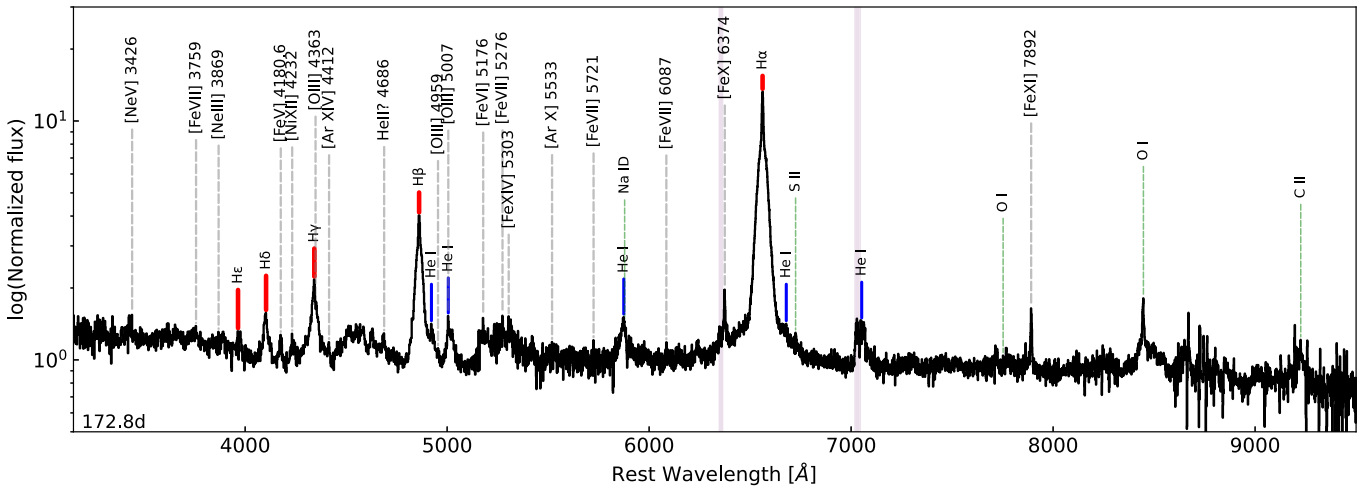

Figure 6. Line identification. The position of each spectral line is marked with vertical lines and the corresponding ion label at the top of each one. Shaded regions show areas affected by telluric lines.

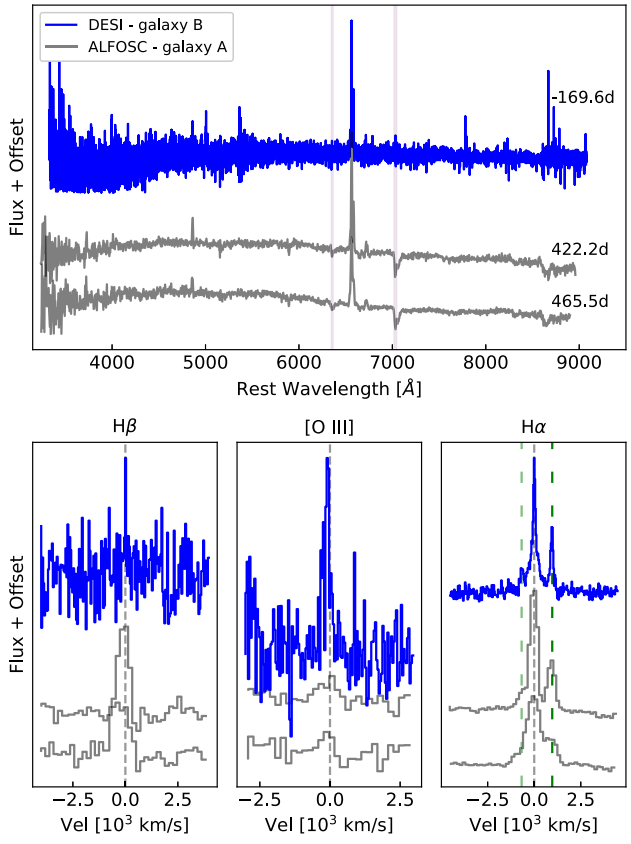

Figure 7. Host spectra normalized to the continuum. Top panel: DESI spectrum obtained at galaxy B ∼ 170 d prior to peak in blue. ALFOSC spectra obtained over 400 d after peak at galaxy A in grey. Shaded areas show the telluric region. Bottom panel: zoom in to the H β, [O III] λ5007 and H α lines (left to right, respectively). Grey vertical dashed lines show respective rest velocities. Green vertical dashed lines in the rightmost panel mark the position of the [N II] λ6548 and λ6584.

58 d after peak. The following observed spectra seem to show little to no spectral line evolution. In Fig. 6, we show the identified spectral lines on the spectrum obtained at ∼ 173 d. Besides the hydrogen lines that originally led to the Type II SN classification, we can see several lines from He I. In particular, the He I λ5876 is blended with Na ID. It is unclear whether Fe II lines are present at λ4924 and λ5018, as they overlap with He I λ4922 and λ5016, respectively. There is also weak S II λ6715 and possibly C II λ9234, although the redder part of the spectrum is quite noisy, making it difficult to properly identify lines. We see O I λ8446 but there is barely any indication of O I λ7774. The absence of O I λ7774 and presence of O I λ8446 could indicate the presence of Bowen resonance-fluorescence mechanisms, which may indicate the existence of intense far-UV radiation fields (see Osterbrock & Ferland 2006). We tentatively identify He II λ4686. In addition, we see several high excitation lines, such as [Ne V] λ3426, [Ne III] λ3869, [Fe VII] λ3759, [Fe V] λ4180.6, [Ni XII] λ4232, [O III] λ4363, [Ar XIV] λ4412, [O III] λ4959, [O III] λ5007, [Fe VI] λ5176, [Fe VII] λ5276, [Fe XIV] λ5303, [Ar X] λ5533, [Fe VII] λ5721, [Fe VII] λ6087, [Fe X] λ6374, and [Fe XI] λ7892. Some of these lines are typically known as coronal lines, and require intense UV/X-ray radiation or collisionally ionized hot gas to be formed (see Osterbrock & Ferland 2006). The spectra show little evolution and the same lines can be identified during most of the spectral sequence.

3.3 Host

AT2022rze has been ingested by the `Blast` web application[11] (Jones et al. 2024), which provides global and local (within 2 kpc) properties of a transients' host galaxy. The software uses UV, optical and IR archival data of the host to fit the spectral energy distribution (SED) and estimate different characteristics. `Blast` considers the (global) host galaxy of AT2022rze to be enclosed by the green ellipse shown in the top right panel of Fig. 1. Throughout this work, we have been considering that to be the host of AT2022rze, WISEAJ122252.07+760253.9.

Images from many shallow surveys (including *WISE*) suggest that host WISEAJ122252.07+760253.9 has an irregular morphology. A visual inspection of deeper images from the Legacy Survey suggest that this is because it is formed by two separate galaxies undergoing a merging event (see Fig. 1). To explore this possibility and better

[11] https://blast.scimma.org/

understand the transient's location within its host, we perform a qualitative analysis of the Legacy Survey r band image shown in the top right panel of Fig. 1. We first displayed the image on the SAOImage DS9 software (Smithsonian Astrophysical Observatory 2000; Joye & Mandel 2003), considering an intensity range from −0.1 to 0.6. Then, we used the contours analysis tool to find the curves defined by constant value pixels, and find two different regions of maximum intensity, indicating that the host is a merging system.

To be consistent with the above, we will still consider the host to be the overall merging system. This is, we will still call host to the area contained by the green ellipse in Fig. 1. The centre of the host defined in this way is RA = $12^{h}22^{m}52^{s}.04$, Dec. = $+76°02'52''.03$, this is 1.9 arcsec away from the WISEAJ122252.07+760253.9 coordinates reported on NED. The host is formed by galaxy A and galaxy B (for 'blob'), the nuclear regions of which are marked by dashed cyan and orange ellipses, respectively, in Fig. 1. These ellipses were obtained by fitting the contours found by the SAOImage DS9 software. The centre of galaxy A is RA = $12^{h}22^{m}51^{s}.944$, Dec. = $+76°02'52''.643$. The centre of galaxy B is RA = $12^{h}22^{m}52^{s}.155$, Dec. = $+76°02'47''.401$.

The location of AT2022rze is then offset 4.8 arcsec (7.1 kpc), 5.4 arcsec (8.1 kpc) and 0.1 arcsec (0.2 kpc) from the centre of the host, the centre of galaxy A and the centre of galaxy B, respectively. This is a rough approximation and dedicated analysis of deeper, higher resolution images are needed to better locate the transient. Still, the host galaxy appears to be a galaxy merger with disturbed morphology and AT2022rze appears coincident with one of the nuclei of this galaxy merger (identified as galaxy B).

The `Blast` analysis concludes that the host of AT2022rze is consistent with an AGN, both in their global and local properties, even though the latter only include optical bands. Note that the global analysis includes the entirety of the host while the local analysis only includes galaxy B (see upper right panel of Fig. 1). While the `Blast` approach has some limitations (see Jones et al. 2024), it offers a useful and efficient means of rapidly assessing the host galaxy and estimating its properties. The parameters inferred for AT2022rze can be found at https://blast.scimma.org/transients/2022rze/. Most relevant to decipher the nature of AT2022rze are: the estimated median mass, which is 5.5×10^{10} $M_{\odot}$ for the global analysis, and 4.9×10^{9} $M_{\odot}$ for the local analysis; the estimated star formation rate, which is 4.3 and 0.03 $M_{\odot}$ y^{-1} for the global and local analysis, respectively; and the AGN role (or f_{AGN}, fraction of bolometric luminosity emission due to AGN), which is 1.9 per cent and 18 per cent for the global and local analysis, respectively. These parameters indicate that the host is a massive galaxy with a moderate star formation and a very weak influence of an AGN. On the contrary, the local analysis is consistent with a low-mass galaxy (similar to a dwarf galaxy), with very low star formation and a non-negligible probability of AGN activity. Although this analysis is limited and insufficient to securely claim the presence of an AGN, and the local photometry would need to be deconvolved to accurately estimate the mass of both galaxies, the differences between the global and local analysis, together with the qualitative assessment of the morphology of the galaxy, indicates that galaxy B, at which AT2022rze is centred, is indeed a smaller galaxy with a nuclear AGN merging with a bigger, star-forming galaxy.

Galaxy B was observed by DESI a few months before AT2022rze went off. The spectrum is rather noisy (see Fig. 7). When compared to our ALFOSC spectra obtained at the centre of galaxy A, we can see that the Hβ feature of galaxy B is narrower and the [O III] λ5007 feature is much stronger than that seen in galaxy A (bottom panel of Fig. 7).

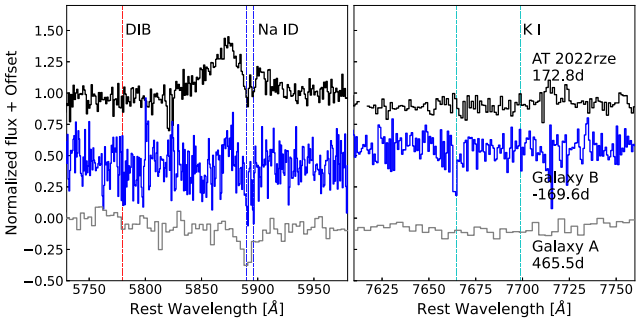

Figure 8. Spectral lines associated with host extinction. The top spectrum in black corresponds to AT2022rze , the middle spectrum in blue correspond to galaxy B, and the bottom spectrum in grey corresponds to galaxy A.

Although we do not consider host extinction for AT2022rze, we can see Na ID absorption lines both in the transient and in the host (see Fig. 8). It has been argued that the pseudo-equivalent width (pEW) of these lines can be used to estimate the associated host extinction as

$$log10(E(B-V)) = 1.17 \times pEW(D1+D2) - 1.85 \pm 0.08, \quad (2)$$

where pEW(D1 + D2) is the sum of the pEW of both Na ID components (Poznanski, Prochaska & Bloom 2012). This method has several caveats and becomes insensitive at pEW(Na ID) $\gtrsim$ 1Å (Phillips et al. 2013). From the spectrum of AT2022rze, we obtain pEW(D1) = 1.1 ± 0.4 Å and pEW(D2) = 0.6 ± 0.3 Å; this is consistent with the pEW of the same lines in the galaxy spectra. Thus, attempts to estimate host extinction using this method would be inadequate. Phillips et al. (2013) also consider the diffuse interstellar band (DIB) λ5780 and the K I lines λ7665 and λ7699 as proxy for independently estimating host extinction. We do not clearly see these lines neither on the transient nor on the galaxies (see Fig. 8). Still, we measure a Balmer decrements $f_{H\alpha}/f_{H\beta} > 3.1$ at all phases (see Fig. 12 and Table B2), which is typically indicative of extinction.

Given that there is evidence of host extinction, we decided to consider equation (2), even if inadequate, to provide a rough estimate of the possible impact of such extinction. We obtained a host extinction of $E_{B-V} = 1.38 \pm 0.08$ mag that, considering $R_V = 3.1$, implies an $A_{V\,host} \sim 4.3$ mag. This would imply a peak absolute magnitude of ~ -24.5 mag (∼4 mag brighter than without considering host extinction) and total radiated energies of $E_{rad} \gtrsim 1.4 \times 10^{52}$ erg (considering the pseudo-bolometric peak, see Section 3.1.3), similar to the radiated energy of other ambiguous transients (e.g. Kankare et al. 2017; Mattila et al. 2018).

The colour of AT2022rze also significantly changes when considering host extinction. The observed $g-r$ colour is presented in the left panel of Fig. 4, while the absolute magnitude g and r light curves are presented in the right panel of the same figure. Inspecting the light curves before applying host extinction (circles), we would conclude that AT2022rze is rather red, and definitely redder than TDEs at early times. However, after applying the estimated host extinction, the transient (stars) becomes much bluer. Given our approximations, the true host galaxy extinction would likely be somewhere between these two extremes. In order to effectively determine the host extinction, we would need better resolution spectra, to be able to identify and measure the column density of the extinction indicators. Still, our rough estimation suggests that AT2022rze may be bluer than observed.

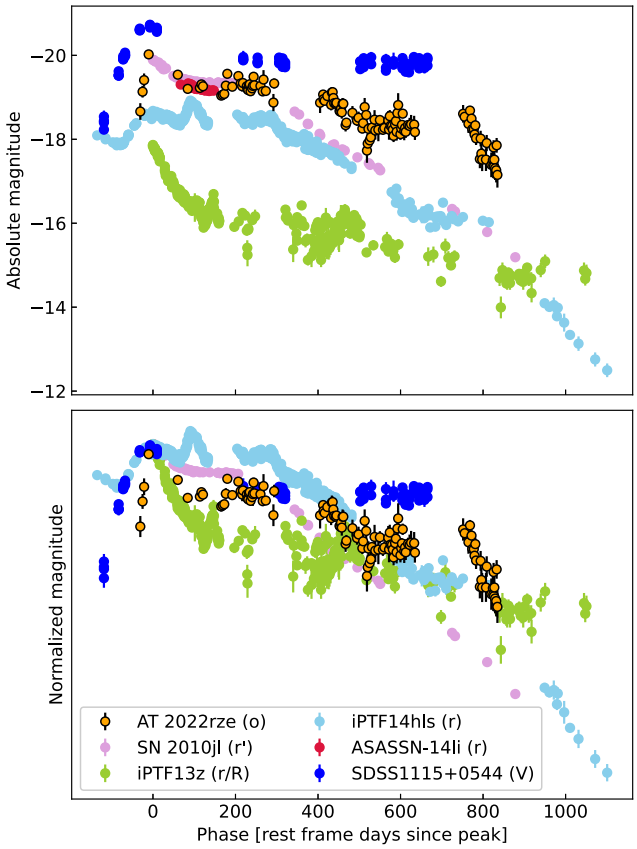

Figure 9. Light curve comparisons. Top panel: Absolute magnitude versus phase with respect to the corresponding light curve peak. Bottom panel: Same as top panel but normalized light curves with respect to peak absolute magnitude.

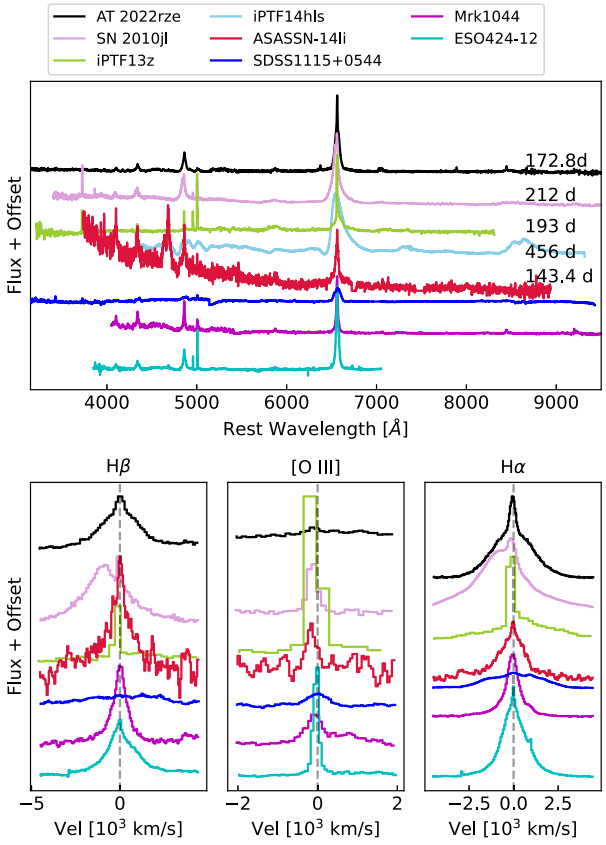

Figure 10. Spectroscopic comparisons. Spectra normalized to the respective continuum. Top panel: Normalized optical spectra. Bottom panel: Zoom in on the three main lines used to classify SNe and AGNs, namely H β on the left panel, [O III] λ5007 on the central panel, and H α on the right panel.

3.4 Comparison to other events

Although AT2022rze was classified as a SN and shows some SN characteristics, it was later classified as an AGN. Yet, both classifications are based on spectral characteristics, which highlights the uncertainties present when performing spectral matching. When the classification between SN and AGN is dubious, one should also consider the possibility of a TDE, as these nuclear transients can also appear similar. Below we compare AT2022rze to well-studied events, including SNe (SN 2010jl, Fransson et al. 2014; iPTF13z, Nyholm et al. 2017; iPTF14hls, Arcavi et al. 2017; Sollerman et al. 2019), AGNs (Mrk1044 and ESO424-12 both obtained from the BAT AGN Spectroscopic Survey[12]), and TDEs (SDSS1115 + 0544, originally considered a CLAGN by Yan et al. 2019; it was re-classified as a TDE by Wang et al. 2022 and Zhang et al. 2025; ASASSN-14li, Holoien et al. 2016; Charalampopoulos et al. 2022) that show similarities, either in the light curve or spectra, to AT2022rze. We also include comparisons to samples of (SL)SN IIn (Taddia et al. 2013; Salmaso et al. 2025), TDEs (Charalampopoulos et al. 2022), and CLAGNs (Zeltyn et al. 2024; Wang et al. 2024b).

Fig. 9 shows the optical light curves of the considered comparison events (except Mrk1044 and ESO424-12 for which we do not have optical light curves). There is a large diversity among the light curves and a qualitative analysis is not enough to claim that AT2022rze is more similar to one event than to another. Compared to Type IIn SN 2010jl, AT2022rze shows a similar peak absolute magnitude and duration before a main steep decline, although the light curve of AT2022rze is 'bumpier'. In that sense, AT2022rze is similar to Type IIn iPTF13z, although the latter is not as luminous, and its bumps are more pronounced. The same is true when comparing to Type II iPTF14hls, although the late time decline of AT2022rze shows some resemblance to the late time decline of the former. SDSS1115 + 0544 is more luminous than AT2022rze and its rise to peak is smoother, its overall light curve seems not to be as bumpy as that of AT2022rze, although the light curve coverage is poorer. Unfortunately, the sampling of the light curve of ASASSN-14li is very limited. Still, we can see similar absolute magnitudes to those seen right after peak in AT2022rze.

Fig. 10 shows spectral comparison between AT2022rze and the considered comparison events. Most objects show similar narrow lines, except iPTF14hls, that shows a typical Type II SN Hα P-Cygni profile, and SDSS115+0544, which has broader H α and H β emission lines. In the bottom panel of Fig. 10, we show a zoom into the Hβ, [O III] λ5007, and Hα profiles. We exclude iPTF14hls here as its lines, typical of a regular SN II, are much broader than for the rest of the sample. The H features of AT2022rze are more symmetrical with respect to rest velocity than the lines of the comparison SNe. In this sense, these features are more similar to those of the comparison AGNs and TDEs, although the broad component of these features is more pronounced for AT2022rze. The [O III] λ5007 feature of every comparison event is stronger than that of AT2022rze.

[12]BASS: https://www.bass-survey.com/

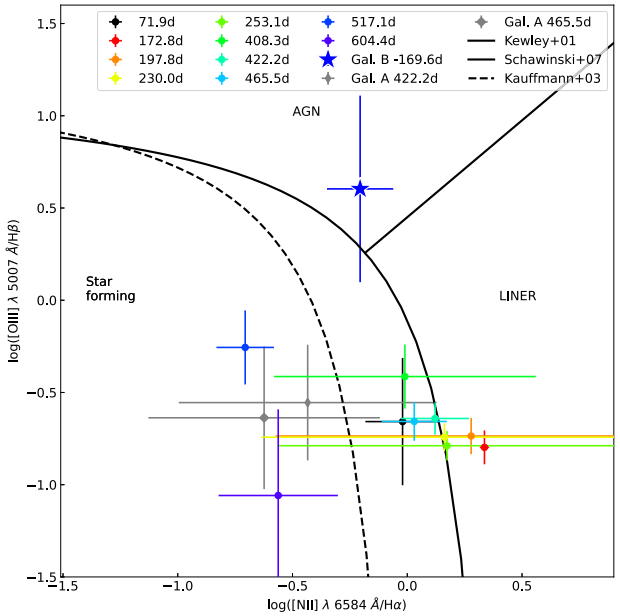

Figure 11. BPT diagram. The black lines delimiting each region are based on models by Kewley et al. (2001), Schawinski et al. (2007), and Kauffmann et al. (2003).

These three lines are of particular interest because, together with [N II] λ6584, can be used as AGN diagnostic when plotting corresponding ratios in a BPT diagram (Baldwin, Phillips & Terlevich 1981). We caution that [N II] λ6584 is not clearly visible in the spectra of AT2022rze, even though it is present in the spectra of the host (see Fig. 7). We assume that the [N II] lines are blended with H α and use the PYTHON package LMFIT (Newville et al. 2024) to fit the H α using a three Gaussian model. We centre one of the Gaussians at the H α rest wavelength and the other two at the rest wavelengths of [N II] λ6548 and λ6584, respectively. We consider the sigma of [N II] λ6584 to be the same of the [O III] λ5007 line (as forbidden lines should have similar dispersion). The results are presented in Fig. 11. While BPT diagrams are known to suffer from biases related to H distribution within galaxies (e.g. Trump et al. 2015) and their applicability to transient phenomena remains uncertain (e.g. Frederick et al. 2019), they can nonetheless provide useful additional context when interpreting events. The measurements for AT2022rze span a broad range that includes the regions corresponding both to star-forming galaxies and liners, the latter formed both by weak AGNs and galaxies that no longer form stars. All the relevant lines are clearly visible in the host spectra, and measurements are straightforward. Galaxy A (grey markers) is consistent with a star forming galaxy, while galaxy B is consistent with an AGN.

WISE colours can also be used as diagnostic to determine whether an event may be an (obscured) AGN (see Wright et al. 2010b). In particular, a single epoch $W1 - W2 \gtrsim 0.5$ mag colour could suggest an AGN origin if it is accompanied by a $W2 - W3 \gtrsim 2.5$ mag. The AllWISE $W1 - W2$ colour measured near the position of AT2022rze before it went off are < 0.5 mag (see Table 1). In particular, the colour corresponding to the position closer to the transient (labelled 'other' in Table 1) is $W1 - W2 = 0.3$ mag. This value is similar to the colours measured for CLAGNs (Frederick et al. 2021). That being said, the *WISE* light curve luminosity (see Fig. 2 and Section 4.3 for further discussion) is comparable to the luminosity observed in other CLAGNs and ANTs (López-Navas et al. 2023; Hinkle 2024). ANTs are ambiguous transients associated to either CLAGNs or obscured TDEs (Wiseman et al. 2025). Distinguishing between the two is challenging, and some previously classified CLAGNs have been reclassified as TDEs, as is the example of SDSS1115 + 0544 (Yan et al. 2019; Wang et al. 2022; Zhang et al. 2025).

Grotova et al. (2025) present a sample of TDEs detected with eROSITA. The eROSITA detection of AT2022rze is fainter than their TDE sample. However, their $W1 - W2$ cut to remove AGNs is similar to that measured for AT2022rze. TDEs are associated with massive black holes (MBHs) with masses $M_{\rm BH} \lesssim 10^8$ M$_\odot$ (although higher masses are possible for highly spinning BHs and low-density stars; Kesden 2012; Leloudas et al. 2016). Yao et al. (2023) present a relation between the host galaxy stellar mass and the mass of the MBH producing the TDE. Considering the local galaxy stellar mass presented in Section 3.3, we infer a BH mass $M_{\rm BH} \sim 7.9 \times 10^5$ M$_\odot$. Considering the relation between BH mass and galaxy stellar mass presented by Reines & Volonteri (2015), we find $M_{\rm BH} \sim 1.2 \times 10^6$ M$_\odot$. These values indicate that a TDE is possible. While not conclusive, these values are much lower than those presented by Reines & Volonteri (2015) for their AGN sample. However, the population of obscured AGN associated with lower-mass BHs is increasing (e.g Purohit, Hickox & Petter 2025).

Fig. 12 shows a comparison of the H α to H β ratio (top panel) and H α full width at half-maximum (FWHM) velocity (bottom panel) of AT2022rze to samples of TDEs, (SL)SNe IIn and CLAGNs. The H α FWHM velocity of AT2022rze was obtained by fitting Gaussian models with LMFIT. The associated error bars were calculated by arbitrarily modifying the limits of the line continua and repeating the Gaussian fit. The corresponding measured parameters for AT2022rze are listed in Table B2. In this case, we only focus on comparison events studied in bulk, as they are analysed using consistent methods and are likely to involve fewer biases than a collection of results obtained from individual object analyses. We selected the TDE sample of Charalampopoulos et al. (2022), the sample of SN IIn of Taddia et al. (2013), the sample of strongly interacting (SI-) SN IIn of Salmaso et al. (2025) that includes two SLSN IIn,[13] and the CLAGN samples of Wang et al. (2024b) for Hα to H β ratio and Zeltyn et al. (2024) for H α FWHM velocity. The relevant parameters of CLAGNs are taken from two separate studies, as we did not find a single work that provides both. Furthermore, we show only the highest and lowest measurements of each parameter as a shaded region, since the considered studies do not account for different light curve phases. Note that the considered phases also vary from study to study, we present rest frame days since peak similar to Charalampopoulos et al. (2022), although they consider peaks at different bands. Taddia et al. (2013) consider days since discovery and Salmaso et al. (2025) days since explosion. Thus a phase shift of up to 90 d (largest rise time upper limit in Salmaso et al. 2025) may need to be consider for the SN IIn comparison samples.

In the top panel of Fig. 12, we can see that the H α to Hβ ratios of AT2022rze are among the highest values measured for TDEs and SN IIn, and are consistent with the values measured for SI-SN IIn at later times. The comparison to CLAGN is somewhat unfair as our measurements consider the entire observed spectrum and the CLAGN measurements of Wang et al. (2024b) subtract the galaxy component, so they represent only a lower limit in this case. In the bottom panel of Fig. 12, we can see that the measured H α

[13]We consider SLSN II any Type II event whose light curve reach a peak magnitude brighter than −20 mag (Pessi et al. 2025).

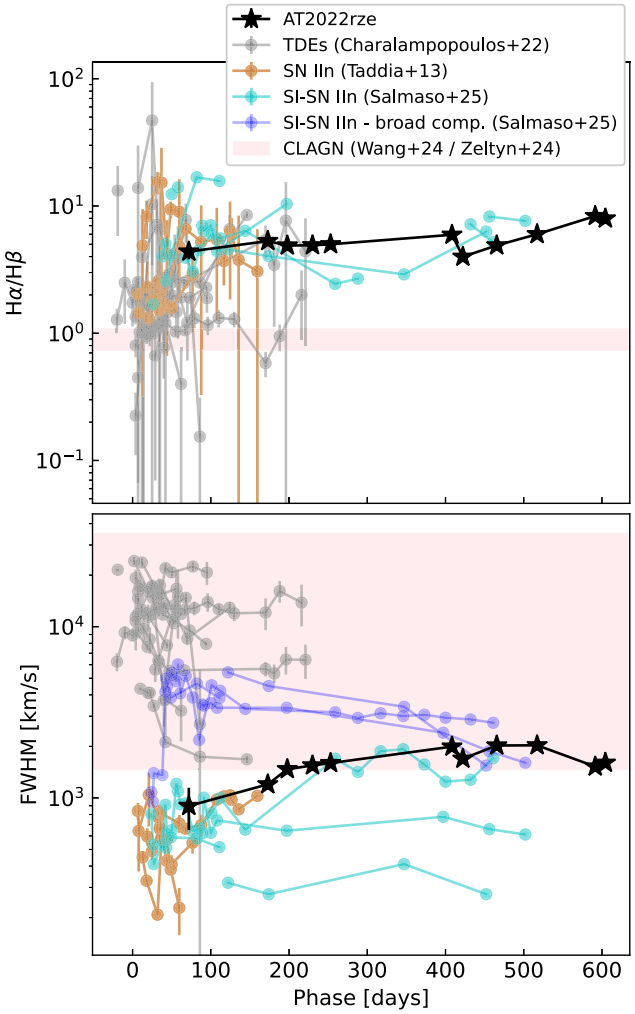

Figure 12. Comparison of AT2022rze to samples of TDEs, SNe IIn, and CLAGNs. Top panel: Hα to Hβ ratio. Bottom panel: Hα FWHM velocity. AT2022rze is presented as black stars. The sample of TDEs of Charalampopoulos et al. (2022) is presented in grey. The sample of SN IIn of Taddia et al. (2013) is presented in brown. The parameters for the narrow component features of the sample of Salmaso et al. (2025) are presented in cyan and the broad components in blue. Pink regions mark the higher and lower values of the Hα to Hβ ratio and Hα velocity of the samples of Wang et al. (2024b) and Zeltyn et al. (2024), respectively. Note that these pink regions include measurements that do not consider light curve phases.

velocity for AT2022rze is much lower than the velocities measured for the considered sample of TDEs. At early times, the velocity of AT2022rze is consistent with the velocity of the narrow components of SN IIn and SI-SN IIn. Both Taddia et al. (2013) and Salmaso et al. (2025) present measurements for the broad and narrow components of the Hα features, if these are distinguishable. We only consider the velocity of the narrow component of the sample of Taddia et al. (2013) as it provides a good enough fit to the features they present. The sample of Salmaso et al. (2025) show significantly broader features so we include both the narrow and broad components separately. At late times the broad Hα component velocity of SI-SN IIn is comparable to that of AT2022rze, while the rest of the events show slower narrow component velocities, except for SN 2021acya. The CLAGNs' lower Hα velocities are also consistent with the late time velocities of AT2022rze.

4 DISCUSSION

AT2022rze is a puzzling transient event that share characteristics with SLSNe II, AGNs, and TDEs. Below, we explore the implications of our analysis within the context of each of these possible scenarios.

4.1 SLSNe II

AT2022rze was originally classified as a H-rich SN based on the presence of narrow Balmer lines. We show in Section 3.3 that the position of the transient (galaxy B, see Fig. 1) may be associated to an AGN. This association does not exclude the possibility of a SN. On the contrary, it has been proposed that the rates of CCSNe are the same or even higher in AGNs or star-forming galaxies (Petrosian & Turatto 1990; Petrosian et al. 2005).

In SNe, the presence of narrow lines indicate CSM interaction. Its bumpy light curve is also consistent with the presence of CSM, and it is reminiscent of other long-lived H-rich events (see Section 3.4). It has been argued that these bumpy, long-lived light curves result from the interaction between the SN ejecta and a CSM with large density variations. Such a CSM structure can be produced by episodic mass-loss events. These are often associated with Luminous Blue Variable-like progenitors (e.g. Smith et al. 2011) or Pulsational Pair Instability SNe (PPISNe, e.g: Woosley 2017, 2018).

At early times, the observed colours of AT2022rze agree more with those observed for SLSNe II than for TDEs (see Fig. 4). The estimated total radiated energy (see Section 3.1.3) can be explained by CSM interaction. However, a rough analysis of the impact of the potential host extinction indicates that the transient may be rather blue (see Section 3.3) and much more energetic, reaching energies of the order of 10^{52} erg. This would present a challenge to an SN interpretation, as the radiated energy would exceed what is available in a neutrino-driven core-collapse explosion (Janka 2012). In this case, the rotational energy of a central engine would be required, in addition to CSM interaction to produce the spectral signatures and the structure in the light curve (Woosley 2017).

The spectra of AT2022rze show several coronal lines (see Section 3.2), with [Fe VII] λ6087, [Fe X] λ6374, and [Fe XI] λ7892 being the strongest ones. Coronal lines are uncommon in SN although not previously unseen in SN IIn (e.g. Fransson et al. 2002; Izotov & Thuan 2009; Smith et al. 2009), where X-rays from the SN excite the CSM. Yet, it has been argued that coronal line emitting transients are associated to TDEs (e.g. Hinkle, Shappee & Holoien 2024) and AGN (e.g. Rose, Elvis & Tadhunter 2015).

4.2 TDE

TDEs are characterized for their blue colours and broad Balmer lines without a blueshifted absorption. AT2022rze show red colours unless we consider high host extinction (see Fig. 4). In addition, The Hα line are much narrower than those in other TDEs (see Fig. 12). We calculate the time to and from half-peak ($t_{rise,1/2} = 23.7 \pm 0.6$ and $t_{dec,1/2} = 73.6 \pm 0.6$, respectively), and compare them to the same values presented for TDEs by Yao et al. (2023). We find that the half-peak rise and decline time of AT2022rze is similar to those of TDEs, with AT2022rze being among the TDEs with the longest rest-frame duration above half-peak. We note, however, that it is possible that galaxy B hosts an AGN, and it is unclear what the characteristics of the TDE associated with an AGN should look like (Zabludoff et al. 2021).

The host galaxy of AT2022rze is experiencing a merger. Although a few TDEs have been suggested to be associated to merging galaxies

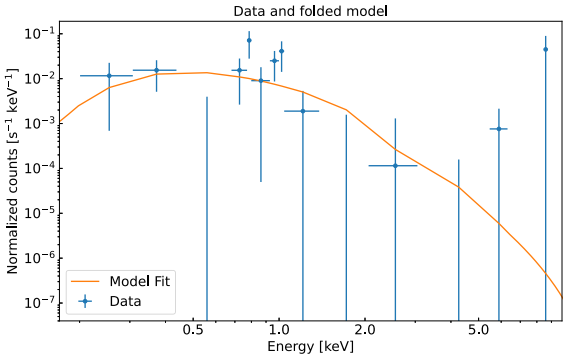

Figure 13. X-ray spectrum fit.

(e.g. Mattila et al. 2018; Kool et al. 2020; Reynolds et al. 2022), there are only two confirmed TDEs in optical wavelengths in such systems (Charalampopoulos et al. 2024; Onori et al. 2025). These events exhibit much smoother light curves and spectroscopic features that differ significantly from those of AT2022rze, making direct comparison unwarranted.

4.3 (CL)AGN

It is often difficult to differentiate between CLAGNs and TDEs due to their overlapping observational features. It has even been proposed that CLAGN are triggered by TDEs (Merloni et al. 2015; Wang et al. 2024a). The analysis of the DESI spectrum of galaxy B, together with the `Blast` analysis, suggest that galaxy B is associated with an AGN.

Using C-statistics (Cash 1979) to model the eROSITA spectrum with an absorbed power-law (`tbabs*cflux*powerlaw` in XSPEC, see Fig. 13), with the Galactic column density fixed at $N_{\rm H} = 3.25 \times 10^{20}\,{\rm cm}^{-2}$ (HI4PI Collaboration 2016), we find a decent fit with `cstat/dof = 18.1/11`, a photon index of $\Gamma = 2.5 \pm 0.7$ and an unabsorbed 0.3–2.3 keV flux of $\log[f_{\rm X}/({\rm erg\,s^{-1}\,cm^{-2}})] = -13.53 \pm 0.13$. The latter corresponds to an X-ray luminosity of $\log[L_{\rm X}/({\rm erg\,s^{-1}})] = 41.67 \pm 0.13$, which is on the fainter end of AGN, consistent with low-luminosity or obscured AGN (Hasinger, Miyaji & Schmidt 2005).

There are several subclassifications of AGN, in particular, they can be divided in radio-loud and radio-quiet (Kellermann et al. 1989). VLASS archival pre-transient images put sub-mJy upper limits near the centre of the host (see Section 2), but there is no radio detection of galaxy B. This suggests a radio-quiet AGN (e.g: Padovani et al. 2009). Radio-quiet AGN are often associated to spiral galaxies, and share many characteristics with star forming galaxies (Bonzini et al. 2013).

Given the evidence of the presence of an AGN at the centre of galaxy B, it is possible that AT2022rze is associated to changes on the environment or accretion rate of said AGN. Considering the transition from the AGN (galaxy B) to the LINER region (earlier spectra of AT2022rze, see Fig. 11), AT2022rze could be considered a CLAGN. CLAGN is a fairly recent and slowly growing class of transients, but the number of events is still low. Their characteristics are very diverse, and their searches can be considered as an anomaly detection task (e.g. Sánchez-Sáez et al. 2021). Therefore, systematic analysis of their time-scales and overall light curve and spectral characteristics is scarce. López-Navas et al. (2023) developed a method to select CLAGN using multiwavelength observations. Unfortunately, we do not have multiwavelength coverage of AT2022rze itself. Still, the host X-ray flux measured before the transient went off, is consistent with the pre-activity X-ray fluxes that López-Navas et al. (2023) measure for their sample of CLAGNs. In addition, the evolution of $W1-W2$ colour at the position of AT2022rze that goes from < 0.5 mag before it is detected (see Table 1) to $\sim$1.1 mag (see last column of Table A3) for the last observed epoch, is in agreement with the interpretation presented by López-Navas et al. (2023), who argue that this effect is produced by a stronger contribution of hot dust produced by the increase in brightness of the AGN.

We argue in Section 3.3 that the steep Balmer decrement values are associated to significant host extinction. However, there is evidence that the Balmer decrement can depend on the accretion-rate for some AGNs and CLAGNs, in such cases the steep Balmer decrement could be related to ionizing photons with low flux (Wu et al. 2023). The fact that the Balmer decrement evolves with time (see Fig. 12) suggests that other mechanisms are in place in addition to extinction. Still, the fact that coronal lines can be seen during the whole spectra evolution suggests the presence of high energies being in place.

5 CONCLUSIONS

We have studied AT2022rze to try to determine its nature. The host of AT2022rze seems to be formed of two galaxies (A and B) undergoing a merging event. The transient is located in the centre of galaxy B, located south-east of the plane-of-sky geometrical centre of the system. AT2022rze exhibits minimal spectral evolution, consistently displaying narrow Balmer lines alongside various high-excitation features, indicative of a persistent high-energy source. The X-ray luminosity observed near the position of the transient before it went off is much lower than that observed in AGNs (e.g: Elvis et al. 1978, 1990; Serlemitsos, Ptak & Yaqoob 1996), although we note that the observations are off-set from the position of the transient. Coronal lines present in the spectra of AT2022rze suggest the presence of soft X-ray and UV emission. As coronal lines are found in AGNs, TDEs, and SNe, their presence alone do not serve as a diagnostic. The overall observed spectroscopic and light curve features of the transient are reminiscent of SLSNe II, TDEs and AGNs.

An analysis of an archival spectrum of galaxy B obtained before AT2022rze occurred suggests that the galaxy is associated with an AGN (see Fig. 11). This is consistent with the environmental analysis performed by `Blast` (see Section 3.3). We roughly estimate the mass of the BH to be between $\sim 1.2 \times 10^6$ and $\sim 7.9 \times 10^5$ $M_\odot$ (see Section 3.3). This does not discard the possibility of an SLSN II or a TDE.

It is worth noting that the sustained presence of coronal lines in the spectra of some transients has led to the proposal of a new class, referred to as coronal line emitters (ECLs). Although this class groups together events that appear to exhibit similar phenomenology, it is not defined by a shared underlying physical mechanism, as the SLSN, TDE, or AGN classes are. Although ECLs have been mostly associated with TDEs (Hinkle et al. 2024), it is still not clear what is their association to CLAGNs (Clark et al. 2024, 2025).

We find possible evidence of Bowen resonance-fluorescence (see Section 3.2). The number of events displaying Bowen fluorescence features has been steadily increasing and a new class of transients dubbed Bowen fluorescence flares has been proposed (BFFs; Trakhtenbrot et al. 2019). Again, this class is defined by observational characteristics rather than by an underlying physical mechanism, and the nature of these transients is still debated (e.g. Śniegowska et al. 2025).

AT2022rze is a luminous ambiguous transient in the nucleus of a merging galaxy. Many such ambiguous events have recently been found and have been dubbed ANTs (Wiseman et al. 2025), which is

another phenomenological class. Wiseman et al. (2025) propose that ANTs could be TDEs produced by different mechanisms than that of standard TDEs.

The estimated total radiated energy of AT2022rze would be difficult to explain in a SLSN II scenario, in particular if we consider significant host extinction (see Section 3.3). Although we cannot discard the possibility of AT2022rze being an unusual TDE, given the closeness of AT2022rze to the nucleus of galaxy B (~ 0.2 kpc), the low Hα FWHM velocities (see Fig. 12), the overall red colours and long duration of the light curve, the increase in $W1-W2$ colour, and the steep Balmer decrement (see Fig. 11), make us conclude that AT2022rze is most likely a CLAGN, triggered by the ongoing merger in its host galaxy.

Panoramic surveys continue to uncover an ever increasing number of ambiguous transients. To disentangle and accurately classify the most luminous events, those that lie at the intersection of SLSNe II, AGN, and TDEs, comprehensive multiwavelength follow-up and systematic comparative analysis are essential. Classification is not merely a matter of labelling; it provides critical insight into the underlying physical mechanisms powering these phenomena. The difficulty in confidently assigning these events to a specific class underscores the current limitations in our understanding of the energetic processes linked to MBHs.

ACKNOWLEDGEMENTS

PJP thanks Stephen Thorp, Laureano Martinez, and Alberto Saldana-Lopez for useful discussion. We thank the referee for their constructive comments. The study is funded by the European Union (ERC, project number 101042299, TransPIre). However, views and opinions expressed are those of the author(s) only and do not necessarily reflect those of the European Union or the European Research Council Executive Agency. Neither the European Union nor the granting authority can be held responsible for them. CL is supported by DoE award #DE-SC0025599. CPG acknowledges financial support from the Secretary of Universities and Research (Government of Catalonia) and by the Horizon 2020 Research and Innovation Programme of the European Union under the Marie Skłodowska-Curie and the Beatriu de Pinós 2021 BP 00168 programme, from the Spanish Ministerio de Ciencia e Innovación (MCIN) and the Agencia Estatal de Investigación (AEI) 10.13039/501100011033 under the PID2023-151307NB-I00 SNNEXT project, from Centro Superior de Investigaciones Científicas (CSIC) under the PIE project 20215AT016 and the program Unidad de Excelencia María de Maeztu CEX2020-001058-M, and from the Departament de Recerca i Universitats de la Generalitat de Catalunya through the 2021-SGR-01270 grant. SM acknowledges support from the Research Council of Finland project 350458. FP acknowledges support from the Spanish Ministerio de Ciencia, Innovación y Universidades (MICINN) under grant PID2022-141915NB-C21. AAM and CL are partially supported by DoE award # DE-SC0025599 and Cottrell Scholar Award # CS-CSA-2025-059 from Research Corporation for Science Advancement. This work is based on observations obtained with the Samuel Oschin Telescope 48-inch and the 60-inch Telescope at the Palomar Observatory as part of the Zwicky Transient Facility project. ZTF is supported by the National Science Foundation under grants AST-1440341 and AST-2034437 and a collaboration including current partners Caltech, IPAC, the Weizmann Institute of Science, the Oskar Klein Center at Stockholm University, the University of Maryland, Deutsches Elektronen-Synchrotron and Humboldt University, the TANGO Consortium of Taiwan, the University of Wisconsin at Milwaukee, Trinity College Dublin, Lawrence Livermore National Laboratories, IN2P3, University of Warwick, Ruhr University Bochum, Northwestern University and former partners the University of Washington, Los Alamos National Laboratories, and Lawrence Berkeley National Laboratories. Operations are conducted by COO, IPAC, and UW. The ZTF forced-photometry service was funded under the Heising-Simons Foundation grant 12540303 (PI: Graham). SED Machine is based upon work supported by the National Science Foundation under grant 1106171. The Gordon and Betty Moore Foundation, through both the Data-Driven Investigator Program and a dedicated grant, provided critical funding for SkyPortal. W. M. Keck Observatory access was supported by Northwestern University and the Center for Interdisciplinary Exploration and Research in Astrophysics (CIERA). This work has made use of data from the Asteroid Terrestrial-impact Last Alert System (ATLAS) project. The Asteroid Terrestrial-impact Last Alert System (ATLAS) project is primarily funded to search for near earth asteroids through National Aeronautics and Space Administration (NASA) grants NN12AR55G, 80NSSC18K0284, and 80NSSC18K1575; byproducts of the NEO search include images and catalogues from the survey area. This work was partially funded by Kepler/K2 (grants J1944/80NSSC19K0112 and HST GO-15889) and STFC (grants ST/T000198/1 and ST/S006109/1). The ATLAS science products have been made possible through the contributions of the University of Hawaii Institute for Astronomy, the Queen's University Belfast, the Space Telescope Science Institute, the South African Astronomical Observatory, and The Millennium Institute of Astrophysics (MAS), Chile. We acknowledge ESA Gaia, DPAC and the Photometric Science Alerts Team (http://gsaweb.ast.cam.ac.uk/alerts). This research has made use of the NED, which is funded by the NASA and operated by the California Institute of Technology. This research has made use of the SVO Filter Profile Service 'Carlos Rodrigo', funded by MCIN/AEI/10.13039/501100011033/ through grant PID2020-112949GB-I00. This research has made use of the SVO Filter Profile Service 'Carlos Rodrigo', funded by MCIN/AEI/10.13039/501100011033/ through grant PID2020-112949GB-I00 The National Radio Astronomy Observatory is a facility of the National Science Foundation operated under cooperative agreement by Associated Universities, Inc. This research has made use of the CIRADA cut-out service at cutouts.cirada.ca, operated by the Canadian Initiative for Radio Astronomy Data Analysis (CIRADA). CIRADA is funded by a grant from the Canada Foundation for Innovation 2017 Innovation Fund (Project 35999), as well as by the Provinces of Ontario, British Columbia, Alberta, Manitoba and Quebec, in collaboration with the National Research Council of Canada, the US National Radio Astronomy Observatory and Australia's Commonwealth Scientific and Industrial Research Organisation. The Legacy Surveys consist of three individual and complementary projects: the Dark Energy Camera Legacy Survey (DECaLS; Proposal ID 2014B-0404; PIs: David Schlegel and Arjun Dey), the Beijing-Arizona Sky Survey (BASS; NOAO Prop. ID 2015A-0801; PIs: Zhou Xu and Xiaohui Fan), and the Mayall z-band Legacy Survey (MzLS; Prop. ID 2016A-0453; PI: Arjun Dey). DECaLS, BASS, and MzLS together include data obtained, respectively, at the Blanco telescope, Cerro Tololo Inter-American Observatory, NSF's NOIRLab; the Bok telescope, Steward Observatory, University of Arizona; and the Mayall telescope, Kitt Peak National Observatory, NOIRLab. Pipeline processing and analyses of the data were supported by NOIRLab and the Lawrence Berkeley National Laboratory (LBNL). The Legacy Surveys project is honoured to be permitted to conduct astronomical research on Iolkam Du'ag (Kitt Peak), a mountain with particular significance to the Tohono O'odham Nation. NOIRLab is operated by the Association of

Universities for Research in Astronomy (AURA) under a cooperative agreement with the National Science Foundation. LBNL is managed by the Regents of the University of California under contract to the U.S. Department of Energy.

This project used data obtained with the Dark Energy Camera (DECam), which was constructed by the Dark Energy Survey (DES) collaboration. Funding for the DES Projects has been provided by the U.S. Department of Energy, the U.S. National Science Foundation, the Ministry of Science and Education of Spain, the Science and Technology Facilities Council of the United Kingdom, the Higher Education Funding Council for England, the National Center for Supercomputing Applications at the University of Illinois at Urbana-Champaign, the Kavli Institute of Cosmological Physics at the University of Chicago, Center for Cosmology and Astro-Particle Physics at the Ohio State University, the Mitchell Institute for Fundamental Physics and Astronomy at Texas A&M University, Financiadora de Estudos e Projetos, Fundacao Carlos Chagas Filho de Amparo, Financiadora de Estudos e Projetos, Fundacao Carlos Chagas Filho de Amparo a Pesquisa do Estado do Rio de Janeiro, Conselho Nacional de Desenvolvimento Cientifico e Tecnologico and the Ministerio da Ciencia, Tecnologia e Inovacao, the Deutsche Forschungsgemeinschaft and the Collaborating Institutions in the Dark Energy Survey. The Collaborating Institutions are Argonne National Laboratory, the University of California at Santa Cruz, the University of Cambridge, Centro de Investigaciones Energeticas, Medioambientales y Tecnologicas-Madrid, the University of Chicago, University College London, the DES-Brazil Consortium, the University of Edinburgh, the Eidgenossische Technische Hochschule (ETH) Zurich, Fermi National Accelerator Laboratory, the University of Illinois at Urbana-Champaign, the Institut de Ciencies de l'Espai (IEEC/CSIC), the Institut de Fisica d'Altes Energies, Lawrence Berkeley National Laboratory, the Ludwig Maximilians Universitat Munchen and the associated Excellence Cluster Universe, the University of Michigan, NSF's NOIRLab, the University of Nottingham, the Ohio State University, the University of Pennsylvania, the University of Portsmouth, SLAC National Accelerator Laboratory, Stanford University, the University of Sussex, and Texas A&M University.

BASS is a key project of the Telescope Access Program (TAP), which has been funded by the National Astronomical Observatories of China, the Chinese Academy of Sciences (the Strategic Priority Research Program 'The Emergence of Cosmological Structures' grant XDB09000000), and the Special Fund for Astronomy from the Ministry of Finance. The BASS is also supported by the External Cooperation Program of Chinese Academy of Sciences (grant 114A11KYSB20160057), and Chinese National Natural Science Foundation (grants 12120101003 and 11433005). This research used data obtained with the Dark Energy Spectroscopic Instrument (DESI). DESI construction and operations is managed by the Lawrence Berkeley National Laboratory. This material is based upon work supported by the U.S. Department of Energy, Office of Science, Office of High-Energy Physics, under Contract No. DE–AC02–05CH11231, and by the National Energy Research Scientific Computing Center, a DOE Office of Science User Facility under the same contract. Additional support for DESI was provided by the U.S. National Science Foundation (NSF), Division of Astronomical Sciences under Contract No. AST-0950945 to the NSF's National Optical-Infrared Astronomy Research Laboratory; the Science and Technology Facilities Council of the United Kingdom; the Gordon and Betty Moore Foundation; the Heising-Simons Foundation; the French Alternative Energies and Atomic Energy Commission (CEA); the National Council of Humanities, Science and Technology of Mexico (CONAHCYT); the Ministry of Science and Innovation of Spain (MICINN), and by the DESI Member Institutions: www.desi.lbl.gov/collaborating-institutions. The DESI collaboration is honored to be permitted to conduct scientific research on I'oligam Du'ag (Kitt Peak), a mountain with particular significance to the Tohono O'odham Nation. Any opinions, findings, and conclusions or recommendations expressed in this material are those of the author(s) and do not necessarily reflect the views of the U.S. National Science Foundation, the U.S. Department of Energy, or any of the listed funding agencies. This work used data of eROSITA telescope onboard SRG observatory. The SRG observatory was built by Roskosmos in the interests of the Russian Academy of Sciences represented by its Space Research Institute (IKI) in the framework of the Russian Federal Space Program, with the participation of the Deutsches Zentrum für Luft- und Raumfahrt (DLR). The SRG/eROSITA X-ray telescope was built by a consortium of German Institutes led by MPE, and supported by DLR. The SRG spacecraft was designed, built, launched and is operated by the Lavochkin Association and its subcontractors. The science data are downlinked via the Deep Space Network Antennae in Bear Lakes, Ussurijsk, and Baykonur, funded by Roskosmos. The eROSITA data used in this work were processed using the eSASS software system developed by the German eROSITA consortium and proprietary data reduction and analysis software developed by the Russian eROSITA Consortium.

DATA AVAILABILITY

The photometric data used in this paper are presented in Appendix A, with except of Gaia photometry that can be found at the dedicated repository at https://gsaweb.ast.cam.ac.uk/alerts/. The spectra can be found on WISeREP at https://www.wiserep.org.

REFERENCES

Arcavi I. et al., 2017, Nature, 551, 210
Baldwin J. A., Phillips M. M., Terlevich R., 1981, PASP, 93, 5
Barnsley R. M., Smith R. J., Steele I. A., 2012, Astron. Nachr., 333, 101
Bellm E. C. et al., 2019a, PASP, 131, 018002
Bellm E. C. et al., 2019b, PASP, 131, 068003
Bilicki M., Jarrett T. H., Peacock J. A., Cluver M. E., Steward L., 2014, ApJS, 210, 9
Blagorodnova N. et al., 2018, PASP, 130, 035003
Blondin S., Tonry J. L., 2007, ApJ, 666, 1024
Bonzini M., Padovani P., Mainieri V., Kellermann K. I., Miller N., Rosati P., Tozzi P., Vattakunnel S., 2013, MNRAS, 436, 3759
Cash W., 1979, ApJ, 228, 939
Charalampopoulos P. et al., 2022, A&A, 659, A34
Charalampopoulos P. et al., 2024, A&A, 689, A350
Chen Z. H. et al., 2023, ApJ, 943, 41
Clark P. et al., 2024, MNRAS, 528, 7076
Clark P. et al., 2025, MNRAS, 540, 871
Coughlin M. W. et al., 2023, ApJS, 267, 31
Dekany R. et al., 2020, PASP, 132, 038001
DESI Collaboration, 2016a, preprint (arXiv:1611.00036)
DESI Collaboration, 2016b, preprint (arXiv:1611.00037)
DESI Collaboration, 2025, preprint (arXiv:2503.14745)
Dey A. et al., 2019, AJ, 157, 168
Elvis M., Fassnacht C., Wilson A. S., Briel U., 1990, ApJ, 361, 459
Elvis M., Maccacaro T., Wilson A. S., Ward M. J., Penston M. V., Fosbury R. A. E., Perola G. C., 1978, MNRAS, 183, 129
Fitzpatrick E. L., 1999, PASP, 111, 63
Förster F. et al., 2021, AJ, 161, 242
Fraga B. M. O. et al., 2024, A&A, 692, A208
Fransson C. et al., 2002, ApJ, 572, 350
Fransson C. et al., 2014, ApJ, 797, 118

Frederick S. et al., 2019, ApJ, 883, 31
Frederick S. et al., 2021, ApJ, 920, 56
Fremling C. et al., 2016, A&A, 593, A68
French K. D., Wevers T., Law-Smith J., Graur O., Zabludoff A. I., 2020, Space Sci. Rev., 216, 32
Gagliano A., 2024, Transient Name Serv. Classif. Rep., 2024-4932, 1
Gagliano A., Contardo G., Foreman-Mackey D., Malz A. I., Aleo P. D., 2023, ApJ, 954, 6
Gaia Collaboration, 2016, A&A, 595, A1
Gal-Yam A., 2017, in Alsabti A. W., Murdin P., eds, Handbook of Supernovae. p. 195
Gal-Yam A., 2019, ARA&A, 57, 305
Gezari S., 2021, ARA&A, 59, 21
Gomez S., Berger E., Blanchard P. K., Hosseinzadeh G., Nicholl M., Villar V. A., Yin Y., 2020, ApJ, 904, 74
Gordon Y. A. et al., 2021, ApJS, 255, 30
Graham M. J. et al., 2019, PASP, 131, 078001
Grishin E., Bobrick A., Hirai R., Mandel I., Perets H. B., 2021, MNRAS, 507, 156
Grotova I. et al., 2025, A&A, 697, A159
Gunn J. E., 1995, in American Astronomical Society Meeting Abstracts #186. p. 44.05
Hasinger G., Miyaji T., Schmidt M., 2005, A&A, 441, 417
HI4PI Collaboration, 2016, A&A, 594, A116
Hinds K., Perley D., Chu M., Dahiwale A., Fremling C., 2022, Transient Name Serv. Classif. Rep., 2022-3514, 1
Hinkle J. T., 2024, MNRAS, 531, 2603
Hinkle J. T., Shappee B. J., Holoien T. W. S., 2024, MNRAS, 528, 4775
Hodgkin S. T. et al., 2021, A&A, 652, A76
Hodgkin S. T. et al., 2022, Transient Name Serv. Discovery Rep., 2022-2428, 1
Hogg D. W., Baldry I. K., Blanton M. R., Eisenstein D. J., 2002, preprint(astro-ph/0210394)
Holoien T. W. S. et al., 2016, MNRAS, 455, 2918
Howell D. A. et al., 2005, ApJ, 634, 1190
Izotov Y. I., Thuan T. X., 2009, ApJ, 707, 1560
Janka H.-T., 2012, Ann. Rev. Nucl. Particle Sci., 62, 407
Jones D. O. et al., 2024, preprint (arXiv:2410.17322)
Joye W. A., Mandel E., 2003, in Payne H. E., Jedrzejewski R. I., Hook R. N., eds, ASP Conf. Ser.Vol. 295, Astronomical Data Analysis Software and Systems XII. Astron. Soc. Pac., San Francisco, p. 489
Kankare E. et al., 2017, Nat. Astron., 1, 865
Kauffmann G. et al., 2003, MNRAS, 346, 1055
Kellermann K. I., Sramek R., Schmidt M., Shaffer D. B., Green R., 1989, AJ, 98, 1195
Kesden M., 2012, Phys. Rev. D, 85, 024037
Kewley L. J., Dopita M. A., Sutherland R. S., Heisler C. A., Trevena J., 2001, ApJ, 556, 121
Kim Y. L. et al., 2022, PASP, 134, 024505
Komossa S., Grupe D., 2024, Serb. Astron. J., 209, 1
Kool E. C. et al., 2020, MNRAS, 498, 2167
Lacy M. et al., 2020, PASP, 132, 035001
Leloudas G. et al., 2016, Nat. Astron., 1, 0002
Li F.-L., Liu Y., Fan X., Hu M.-K., Yang X., Geng J.-J., Wu X.-F., 2023, ApJ, 950, 161
López-Navas E. et al., 2023, MNRAS, 524, 188
Mainzer A. et al., 2011, ApJ, 731, 53
Mainzer A. et al., 2014, ApJ, 792, 30
Mandigo-Stoba M. S., Fremling C., Kasliwal M., 2022, J. Open Source Softw., 7, 3612
Masci F. J. et al., 2019, PASP, 131, 018003
Masci F., 2013, preprint (arXiv:1301.2718)
Mattila S. et al., 2018, Science, 361, 482
Merloni A. et al., 2015, MNRAS, 452, 69
Muthukrishna D., Parkinson D., Tucker B. E., 2019, ApJ, 885, 85
Narayan G. et al., 2018, ApJS, 236, 9
Newville M. et al., 2024, lmfit/lmfit-py: 1.3.2, Zenodo
Nyholm A. et al., 2017, A&A, 605, A6
Oke J. B. et al., 1995, PASP, 107, 375
Oke J. B., Gunn J. E., 1982, PASP, 94, 586
Onori F. et al., 2025, MNRAS, 540, 498
Osterbrock D. E., Ferland G. J., 2006, Astrophysics of Gaseous Nebulae and Active Galactic Nuclei
Padovani P. et al., 2017, A&AR, 25, 2
Padovani P., Mainieri V., Tozzi P., Kellermann K. I., Fomalont E. B., Miller N., Rosati P., Shaver P., 2009, ApJ, 694, 235
Perley D. A., 2019, PASP, 131, 084503
Pessi P. J. et al., 2025, A&A, 695, A142
Petrosian A. et al., 2005, AJ, 129, 1369
Petrosian A. R., Turatto M., 1990, A&A, 239, 63
Phillips M. M. et al., 2013, ApJ, 779, 38
Piascik A. S., Steele I. A., Bates S. D., Mottram C. J., Smith R. J., Barnsley R. M., Bolton B., 2014, in Ramsay S. K., McLean I. S., Takami H., eds, Proc. SPIE Conf. Ser.Vol. 9147, Ground-based and Airborne Instrumentation for Astronomy V. SPIE, Bellingham, p. 91478H
Poznanski D., Prochaska J. X., Bloom J. S., 2012, MNRAS, 426, 1465
Predehl P. et al., 2021, A&A, 647, A1
Prochaska J. et al., 2020a, J. Open Sour. Softw., 5, 2308
Prochaska J. X. et al., 2020b, J. Open Source Softw., 5, 2308
Purohit R. A., Hickox R. C., Petter G. C., 2025, MNRAS, 538, 2116
Rasmussen C. E., Williams C. K. I., 2006, Gaussian Processes for Machine Learning
Reines A. E., Volonteri M., 2015, ApJ, 813, 82
Reynolds T. M., Mattila S., Efstathiou A., Kankare E., Kool E., Ryder S., Peña-Moñino L., Pérez-Torres M. A., 2022, A&A, 664, A158
Ricci C., Trakhtenbrot B., 2023, Nat. Astron., 7, 1282
Rigault M. et al., 2019, A&A, 627, A115
Rodrigo C., Solano E., 2020, in XIV.0 Scientific Meeting (virtual) of the Spanish Astronomical Society. p. 182
Rodrigo C., Solano E., Bayo A., 2012, SVO Filter Profile Service Version 1.0, IVOA Working Draft
Rodríguez Ó. et al., 2019, MNRAS, 483, 5459
Rose M., Elvis M., Tadhunter C. N., 2015, MNRAS, 448, 2900
Salmaso I. et al., 2025, A&A, 695, A29
Sánchez-Sáez P. et al., 2021, AJ, 162, 206
Schawinski K., Thomas D., Sarzi M., Maraston C., Kaviraj S., Joo S.-J., Yi S. K., Silk J., 2007, MNRAS, 382, 1415
Schlafly E. F., Finkbeiner D. P., 2011, ApJ, 737, 103
Schlegel D. J., Finkbeiner D. P., Davis M., 1998, ApJ, 500, 525
Serlemitsos P., Ptak A., Yaqoob T., 1996, in Eracleous M., Koratkar A., Leitherer C., Ho L., eds, ASP Conf. Ser.Vol. 103, The Physics of Liners in View of Recent Observations. Astron. Soc. Pac., San Francisco, p. 70
Shingles L. et al., 2021, Transient Name Server AstroNote, 7, 1
Smith K. W. et al., 2020, PASP, 132, 085002
Smith N. et al., 2009, ApJ, 695, 1334
Smith N., 2017, in Alsabti A. W., Murdin P., eds, Handbook of Supernovae. p. 403
Smith N., Li W., Silverman J. M., Ganeshalingam M., Filippenko A. V., 2011, MNRAS, 415, 773
Smithsonian Astrophysical Observatory, 2000, SAOImage DS9: A utility for displaying astronomical images in the X11 window environment, Astrophysics Source Code Library, preprint(ascl:0003.002)
Śniegowska M. et al., 2025, ApJ, 989, 173
Sollerman J. et al., 2019, A&A, 621, A30
Taddia F. et al., 2013, A&A, 555, A10
Tonry J. L. et al., 2018, PASP, 130, 064505
Trakhtenbrot B. et al., 2019, Nat. Astron., 3, 242
Trump J. R. et al., 2015, ApJ, 811, 26
van der Walt S., Crellin-Quick A., Bloom J., 2019, J. Open Sour. Softw., 4, 1247
Wang S. et al., 2024b, ApJ, 966, 128
Wang Y. et al., 2022, ApJS, 258, 21
Wang Y., Graham M. J., Ford K. E. S., McKernan B., Ryu T., Stern D., 2024a, preprint (arXiv:2406.12096)
Ward C. et al., 2021, ApJ, 913, 102
Wiseman P. et al., 2025, MNRAS, 537, 2024

Woosley S. E., 2017, ApJ, 836, 244
Woosley S. E., 2018, ApJ, 863, 105
Wright E. L. et al., 2010a, AJ, 140, 1868
Wright E. L. et al., 2010b, AJ, 140, 1868
Wu J., Wu Q., Xue H., Lei W., Lyu B., 2023, ApJ, 950, 106
Yan L. et al., 2019, ApJ, 874, 44
Yao Y. et al., 2023, ApJ, 955, L6
Young D. R., 2020, plot_atlas_fp.py, https://zenodo.org/doi/10.5281/zenodo.10978968, access date: 23 May 2023
Zabludoff A. et al., 2021, Space Sci. Rev., 217, 54
Zeltyn G. et al., 2024, ApJ, 966, 85
Zhang Z. et al., 2025, preprint (arXiv:2501.08812)

SUPPORTING INFORMATION

Supplementary data are available at *MNRAS* online.

suppl_data

Please note: Oxford University Press is not responsible for the content or functionality of any supporting materials supplied by the authors. Any queries (other than missing material) should be directed to the corresponding author for the article.

APPENDIX A: LIGHT CURVES

Table A1. ZTF and ATLAS photometry.

MJD (d)	Flux (μJy)	err_Flux (μJy)	ABMag (mag)	err_ABMag (mag)	Filter	Flag
58205.28	0.18	5.46	20.31	···	ZTFg	T
58214.25	−1.38	12.54	19.41	···	ZTFg	T
58216.25	−0.26	4.27	20.58	···	ZTFg	T

Note. The F flag in the last column means real detection and the T flag means upper limit. The full table is available in supplementary material.

Table A2. SEDM photometry.

MJD (d)	ABmag (mag)	err_ABmag (mag)	limiting_mag (mag)	Flux (μJy)	err_Flux (μJy)	Filter
60007.18	19.00	0.32	18.59	91.27	26.55	sdssr
60012.32	18.98	0.07	20.15	93.25	6.31	sdssr
60012.35	···	···	19.44	···	60.96	sdssg
60012.35	···	···	18.10	···	209.65	sdssr
60071.33	18.66	0.15	19.05	124.36	17.36	sdssr
60071.36	···	···	19.53	···	55.87	sdssg
60071.36	18.66	0.09	19.62	124.87	10.26	sdssr
60071.36	17.88	0.05	19.39	255.08	12.75	sdssi
60263.52	18.86	0.07	20.14	103.30	6.40	sdssr
60378.20	20.02	0.10	20.82	35.72	3.42	sdssg
60378.21	19.77	0.06	21.08	45.06	2.68	sdssr
60378.21	18.69	0.04	20.65	120.96	3.98	sdssi
60525.17	19.79	0.09	20.79	44.25	3.50	sdssr
60525.17	18.83	0.05	20.41	106.88	4.97	sdssi
60529.17	19.80	0.07	21.05	43.53	2.75	sdssr
60529.17	18.78	0.04	20.75	111.94	3.63	sdssi
60535.16	···	···	20.69	···	19.23	sdssr
60535.16	18.77	0.04	20.65	112.63	4.00	sdssi
60730.54	···	···	21.20	···	12.04	sdssr
60730.55	19.42	0.07	20.70	61.95	3.82	sdssi

Table A3. *WISE* photometry.

MJD (d)	Flux(W1) (μJy)	err_Flux(W1) (μJy)	Flux(W2) (μJy)	err_Flux(W2) (μJy)	W1_Vega (mag)	err_W1_Vega (mag)	W2_Vega (mag)	err_W2_Vega (mag)	W1_Vega−W2_Vega (mag)
57320.00	31.10	15.00	49.40	25.00	17.09	...	15.90	...	...
57484.00	39.90	15.00	56.50	25.00	17.09	...	15.90	...	...
57687.00	58.30	15.00	77.10	25.00	16.81	...	15.87	...	...
57845.00	47.20	15.00	79.90	25.00	17.04	...	15.83	...	...
58051.00	0.40	15.00	45.00	25.00	17.09	...	15.90	...	...
58208.00	−10.90	15.00	42.50	25.00	17.09	...	15.90	...	...
58415.00	14.90	15.00	32.30	25.00	17.09	...	15.90	...	...
58573.00	−3.40	15.00	92.70	25.00	17.09	...	15.67	...	...
58782.00	2.80	15.00	3.70	25.00	17.09	...	15.90	...	...
58937.00	30.50	15.00	8.00	25.00	17.09	...	15.90	...	...
59147.00	−6.00	15.00	−18.80	25.00	17.09	...	15.90	...	...
59304.00	−11.50	15.00	37.30	25.00	17.09	...	15.90	...	...
59511.00	−8.70	15.00	25.60	25.00	17.09	...	15.90	...	...
59668.00	−16.40	15.00	7.10	25.00	17.09	...	15.90	...	...
59878.00	1732.90	15.00	1700.30	25.00	13.13	0.01	12.51	0.02	0.62
60032.00	2359.40	15.00	2821.20	25.00	12.79	0.01	11.96	0.01	0.83
60242.00	2325.30	15.00	3129.70	25.00	12.81	0.01	11.85	0.01	0.96
60399.00	2128.70	15.00	3215.40	25.00	12.91	0.01	11.82	0.01	1.09

Note. Magnitudes without an associated error bar denote upper limits. AB magnitudes are obtained as W1_AB = W1_Vega + 2.699 and W2_AB = W2_Vega + 3.339, respectively (see https://wise2.ipac.caltech.edu/docs/release/allsky/expsup/sec4_4h.html#conv2flux).

Table A4. Pseudo bolometric light curve.

Phase (d)	$\mathrm{Log_{10}(Lbol)}$ ($\mathrm{erg\,s^{-1}}$)	$\mathrm{err\_Log_{10}(Lbol)}$ ($\mathrm{erg\,s^{-1}}$)
−34.48	42.48	0.06
−34.39	42.49	0.06
−34.29	42.49	0.06

Note. The full table is available in supplementary material.

APPENDIX B: SPECTRAL LOG AND MEASUREMENTS

Table B1. Spectral log.

Target	Date	MJD (d)	phase (d)	Instrument
AT 2022rze	2022-11-16	59899.49	58.24	SEDM
AT 2022rze	2022-12-01	59914.23	71.87	SPRAT
AT 2022rze	2023-03-04	60007.18	157.79	SEDM
AT 2022rze	2023-03-09	60012.32	162.54	SEDM
AT 2022rze	2023-03-20	60023.47	172.84	LRIS
AT 2022rze	2023-04-16	60050.45	197.78	LRIS
AT 2022rze	2023-05-07	60071.33	217.09	SEDM
AT 2022rze	2023-05-21	60085.31	230.01	LRIS
AT 2022rze	2023-06-15	60110.25	253.07	LRIS
AT 2022rze	2023-06-15	60110.31	253.12	LRIS
AT 2022rze	2023-11-15	60263.52	394.74	SEDM
AT 2022rze	2023-11-30	60278.16	408.28	ALFOSC
AT 2022rze	2023-12-15	60293.20	422.18	ALFOSC
AT 2022rze	2024-01-31	60340.04	465.48	ALFOSC
AT 2022rze	2024-03-26	60395.88	517.09	ALFOSC
AT 2022rze	2024-06-15	60476.23	591.37	DBSP
AT 2022rze	2024-06-29	60490.27	604.35	LRIS
Galaxy B	2022-03-15	59653.00	−169.61	DESI
Galaxy A	2023-12-15	60293.20	422.18	ALFOSC
Galaxy A	2024-01-31	60340.04	465.48	ALFOSC

Table B2. Balmer decrement and velocity.

Target	Phase (d)	Hα/Hβ	err_Hα/Hβ	Vel(Hα) ($\mathrm{km\,s^{-1}}$)	err_Vel(Hα) ($\mathrm{km\,s^{-1}}$)
AT 2022rze	58.24	...	...	...	...
AT 2022rze	71.87	4.4	0.6	897.5	248.9
AT 2022rze	157.79	...	...	...	...
AT 2022rze	162.54	...	...	...	...
AT 2022rze	172.84	5.3	0.1	1200.2	7.8
AT 2022rze	197.78	4.9	0.1	1471.6	30.8
AT 2022rze	217.09	...	...	...	...
AT 2022rze	230.01	4.9	0.1	1547.6	1.0
AT 2022rze	253.07	5.0	0.1	1596.9	65.3
AT 2022rze	253.12	...	...	...	...
AT 2022rze	394.74	...	...	...	...
AT 2022rze	408.28	5.9	0.2	1993.4	1.0
AT 2022rze	422.18	4.0	0.1	1693.9	51.4
AT 2022rze	465.48	4.9	0.1	2023.7	139.8
AT 2022rze	517.09	6.0	0.3	2028.8	64.5
AT 2022rze	591.37	8.3	0.2	1524.6	78.4
AT 2022rze	604.35	8.0	0.1	1604.2	36.9
Galaxy B	−169.61	10.4	1.1	...	...
Galaxy A	422.18	3.5	0.8	...	...
Galaxy A	465.48	2.6	0.7	...	...

[1]*The Oskar Klein Centre, Department of Astronomy, Stockholm University, Albanova University Center, SE 106 91 Stockholm, Sweden*
[2]*Caltech Optical Observatories, California Institute of Technology, Pasadena, CA 91125, USA*
[3]*Minnesota Institute for Astrophysics, University of Minnesota, 116 Church Street SE, Minneapolis, MN 55455, USA*
[4]*Miller Institute for Basic Research in Science, 468 Donner Lab, Berkeley, CA 94720, USA*
[5]*Department of Astronomy, University of California, Berkeley, CA 94720, USA*
[6]*Independent Researcher, Sweden*
[7]*Division of Physics, Mathematics and Astronomy, California Institute of Technology, Pasadena, CA 91125, USA*
[8]*Space Research Institute, Russian Academy of Sciences, Profsoyuznaya 84/32, 117997 Moscow, Russia*

[9]*Max Planck Institute for Astrophysics, Karl-Schwarzschild-Str 1, Garching b. München D-85741, Germany*
[10]*Center for Interdisciplinary Exploration and Research in Astrophysics (CIERA), 1800 Sherman Avenue, Evanston, IL 60201, USA*
[11]*The Oskar Klein Centre, Department of Physics, Stockholm University, Albanova University Center, SE-106 91 Stockholm, Sweden*
[12]*European Southern Observatory, Alonso de Córdova 3107, Vitacura, Santiago, Chile*
[13]*Cahill Center for Astrophysics, California Institute of Technology, Pasadena, CA 91125, USA*
[14]*MIT-Kavli Institute for Astrophysics and Space Research, 77 Massachusetts Avenue, Cambridge, MA 02139, USA*
[15]*Astrophysics Research Institute, Liverpool John Moores University, 146 Brownlow Hill, Liverpool L3 5RF, UK*
[16]*Department of Physics and Astronomy, Northwestern University, 2145 Sheridan Road, Evanston, IL 60208, USA*
[17]*NSF-Simons AI Institute for the Sky (SkAI), 172 E. Chestnut Str, Chicago, IL 60611, USA*
[18]*Department of Physics and Astronomy, University of Turku, Vesilinnantie 5, FI-20014, Turku, Finland*
[19]*Institut d'Estudis Espacials de Catalunya (IEEC), Edifici RDIT, Campus UPC, E-08860 Castelldefels (Barcelona), Spain*
[20]*Institute of Space Sciences (ICE, CSIC), Campus UAB, Carrer de Can Magrans, s/n, E-08193 Barcelona, Spain*
[21]*School of Sciences, European University Cyprus, Diogenes Street, Engomi, 1516 Nicosia, Cyprus*
[22]*Aalto University Metsähovi Radio Observatory, Metsähovintie 114, FI-02540 Kylmälä, Finland*
[23]*Aalto University Department of Electronics and Nanoengineering, P.O. Box 15500, FI-00076 Aalto, Finland*
[24]*Instituto de Astrofísica de Canarias, C/Vía Láctea, s/n, San Cristóbal de La Laguna, E-38205 Tenerife, Spain*
[25]*Universidad de La Laguna, Dpto. Astrofísica, San Cristóbal de La Laguna, E-38206 Tenerife, Spain*
[26]*Physics Division, Lawrence Berkeley National Laboratory, 1 Cyclotron Road, MS 50B-4206, Berkeley, CA 94720, USA*
[27]*IPAC, California Institute of Technology, 1200 E. California Blvd, Pasadena, CA 91125, USA*

This paper has been typeset from a TEX/LATEX file prepared by the author.